Wide-Area Monitoring and Control of WECC Transfer Paths Using Real-Time Digital Simulations

Annual Project Report
October 21, 2013

Principal Investigator: Dr. Aranya Chakrabortty
Assistant Professor, Electrical & Computer Engineering
North Carolina State University, Raleigh, NC, USA
Email: achakra2@ncsu.edu

Co-Principal Investigator: Dr. Subhasish Bhattacharya
Associate Professor, Electrical & Computer Engineering
North Carolina State University, Raleigh, NC, USA
Email: sbhatta4@ncsu.edu

Graduate Students: Govind S. Chavan & Matthew D. Weiss
North Carolina State University, Raleigh, NC, USA
Emails: gschavan@ncsu.edu, mdweiss@ncsu.edu

Industry Partners: Armando Salazar & Frank Ashrafi
Southern California Edison, Westminster, CA, USA
Email: armando.salazar@sce.com, farrokh.habibiashrafi@sce.com

List of symbols

A_i:	i^{th} area
P_i:	Pilot bus for the i^{th} area
ASG_i:	Aggregated synchronous generator representing area A_i
$E_i\angle\delta_i$:	Voltage Phasor of the internal EMF of ASG_i
$V_i\angle\theta_i$:	Voltage Phasor at pilot bus P_i
x_i:	Internal Thevenin reactance of ASG_i
r_{ij}:	Resistance of transmission line between P_i and P_j
x_{ij}:	Reactance of transmission line between P_i and P_j
p_{ij}:	Active power flow between buses P_i and P_j
$\tilde{I}_i$:	Current Phasor injected at P_i^{th} bus by ASG_i

1 Introduction

1.1 Project Objective

The objective of this research project is to develop an experimental framework for testing transient stability, frequency response and oscillation damping of the US Western Interconnection using a Real-time Digital Simulator (RTDS). Over the project period we have constructed a reduced-order, 5-machine dynamic equivalent model using Synchronized Phasor Measurements [1, 2] to represent the primary oscillation clusters of the WECC power system, starting from the major generation clusters in Alberta, Washington and Oregon to the load clusters in Southern California, Montana and Arizona with intermediate voltage support at appropriate points, as shown in Figure 1 referenced from [3]. This figure shows the so-called wide-area, clustered view of the WECC system [4, 5], breaking the entire interconnection into several well-defined, coherent generation/load clusters that oscillate with respect to each other in face of different disturbances. Such oscillations between

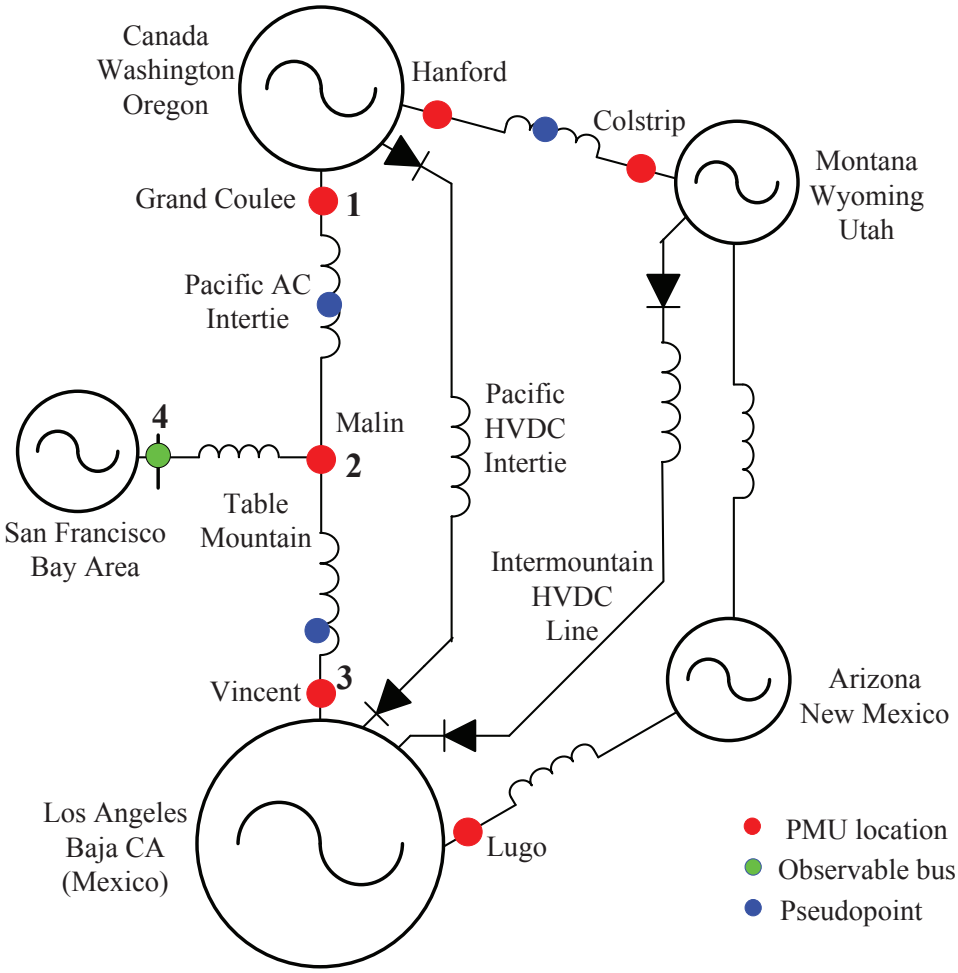

Figure 1: A 5-area dynamic equivalent model for the WECC power system

aggregate clusters are typically referred to as inter-area oscillations, which is well-studied and well-understood for the traditional operating conditions of the WECC. However, with gradual expansion in transmission level infrastructure as well as tremendous penetration of renewable power including wind and solar photovoltaic in the west coast over the next decade, several dynamical properties of the WECC will change significantly, and so will the characteristics of the interarea oscillations and their stability margins [6, 7, 8]. Such projected changes are neither well-understood from an analytical perspective nor well-established from an experimental or validation point of view. Our goal is to bridge this gap by investigating how real-time changes in operating conditions, unforeseen contingencies, and intermittency of renewable generation have an impact on the inter-area oscillations in WECC, and validate those observations using an RTDS-based emulation framework. Our study will be divided into three major phases, answering three major questions as follows:

1. How can Synchrophasor measurements of voltage, phase angle, and frequency collected from a set of critical buses in the WECC can be used to construct a reliable dynamic equivalent model of the entire system capturing the significant inter-area modes of oscillation

2. How can the identified reduced-order model be implemented and validated using a hardware-in-loop real-time digital simulation framework integrated with Phasor Measurement Units

3. How does the implemented model react to different types of contingencies, and how utility companies operating over the different clusters of the WECC can predict their local phase angle responses and prepare for the worst-case contingency happening at any other cluster.

1.2 Motivation and Literature Review

Recent analyses of phase angle and frequency oscillations in the Western Electricity Coordinating Council (WECC) and the Eastern Interconnect (EI) have highlighted the importance of constructing real-time dynamic models of large power systems from Synchrophasor measurements [9]. For example, spectral analysis of phase angles in the California-Oregon Intertie [10], or frequency oscillations between New England and the Entergy grid in Florida [11] clearly indicate the potential use of such predictive models for critical applications such as oscillation monitoring, transient stability assessment, and voltage instability prediction. However, given the large size of any realistic power system, such as the WECC or EI, it is practically impossible to derive the pre-event or post-event dynamic model for the entire network in real-time. System operators are, rather, more interested in constructing reduced-order models of the power system that capture the dominant inter-area modes of oscillation, and, hence, can predict how the different parts of the system may oscillate with respect to each other in the face of a particular event. Such reduced-order models are often referred to as *wide-area* models [13, 12, 14].

Preliminary results for constructing wide-area models of two-area power systems using PMU measurements have recently been presented in [15]. The authors in this paper listed two main steps for deriving these models, namely 1. identification of the dynamic equivalent model for each area, and 2. identification of the topology of the equivalent reduced-order transmission network connecting these areas. The topology identification step was not addressed in [15] as the system under study was a simple two-area system connected by a single tie-line. For multi-area power systems, however, identifying the parameters of the equivalent topology as well as that of the individual equivalent generators becomes absolutely imperative. The topology graph captures the effective impedance between the areas, while the equivalent inertia indicates the relative strength of one area with respect to another, and thereby retains the modal frequencies and the mode shapes for the inter-area oscillations.

Our objective is to identify this equivalent topology and inertial parameters for the five-area WECC model shown in Figure 1 with well-defined inter-area modes using PMU measurements collected from the terminal buses of each cluster. The uniqueness of our approach compared to traditional topology identification methods are as follows:

• First, the majority of network reduction methods used in the power system literature are model-based, such as the methods based on modal equivalencing [16], coherency [17], and decomposition algorithm assigning coupling factors to generators [18]. In contrast, our methods are completely measurement-based, and need only a few basic information about the underlying system model.

• Traditional methods such as SME [21] tend to capture the details of fast local oscillations that may not be necessary for wide-area monitoring but increases the computation time. Our methods, in contrast, are based on inter-area or slow oscillation only and, therefore, will be significantly faster.

• In computer science literature, topology identification of large complex networks is often formulated as a combinatorial optimization problem [22]. Our methods, however, are not based on combinatorial analysis, but follow from underlying system dynamics, thereby preserving all the system-level properties as reflected in the PMU measurements.

• Compared to recent works of [23, 24, 25] on topology identification of generic network dynamic systems using graph-theoretic methods, and of [26] where raw PMU data was used to estimate a Thevenin equivalent model of power systems in steady-state, our approach integrates model reduction with identification by considering separation of slow and fast dynamics.

Once constructed, the inter-area topology can be used for useful applications such as transient stability assessment and voltage stability assessment. For example, a common tool for assessing transient stability of a multi-area power system is the transient energy function consisting of kinetic and potential energies. As shown in [27], the potential energy function is dependent on the inter-area topology. Similarly, this topology can also serve as a critical parameter for tracking loadabilty limits for voltage, wide-area protection, and islanding schemes.

2 Problem Formulation

We first recall the general ideas on how a multi-area power system model can be reduced to its dynamic equivalent via time-scale separation. For this, let us consider a power system network consisting of n synchronous generators and n_l loads connected by a given topology. Without loss of generality, we assume buses 1 through n to be the generator buses and buses $n+1$ through $n+n_l$ to be the load buses. Let P_m denote the vector of the mechanical power injection at generator buses, P_L be the vector of total active power consumed by the loads, and P_i^N be the total active power injected to the i^{th} bus of the network ($i = 1, \ldots, n+n_l$), where the superscript N indicates that this power is flowing in the network as opposed to the loads. This power is calculated as:

$$P_i^N = \sum_{k=1}^{n+n_l} \big(V_i^2 r_{ik}/y_{ik}^2 + V_i V_k \sin(\theta_{ik} - \alpha_{ik})/y_{ik}\big), \tag{1}$$

where, $V_i\angle\theta_i$ is the voltage phasor at the i^{th} bus, $\theta_{ik} = \theta_i - \theta_k$, r_{ik} and x_{ik} are the resistance and reactance of the transmission line joining buses i and k, $y_{ik} = \sqrt{r_{ik}^2 + x_{ik}^2}$, and $\alpha_{ik} = \tan^{-1}(r_{ik}/x_{ik})$. Let P_G^N and P_L^N denote the vectors of P_i^N calculated for generators and loads, respectively. The electromechanical model of the power system can be described as a system of differential-algebraic equations (DAE) [28]:

$$\mathcal{M}\ddot{\delta} = P_m - P_G^N - \mathcal{D}\omega, \tag{2a}$$

$$P_L - P_L^N = 0, \tag{2b}$$

where δ is the vector of generator angles, ω is the vector of the speed deviation of the generators from synchronous speed, and $\mathcal{M} = \text{diag}(M_i)$ and $\mathcal{D} = \text{diag}(D_i)$ are $n \times n$ diagonal matrices of the generator inertias and damping factors, respectively. The DAE (2) can be converted to a system of pure differential equations by relating the algebraic variables V_i and θ_i to the system state variables (δ, ω) from (2b), and then substituting them back in (2a) via Kron reduction. The resulting system is a fully connected network of n second-order oscillators with $l \leq n(n-1)/2$ tie-lines. Let the internal voltage phasor of the i^{th} machine be denoted as $\widetilde{E}_i = E_i\angle\delta_i$. The electromechanical dynamics of the i^{th} generator in the Kron's form, neglecting line resistances, can be written as:

$$\dot{\delta}_i = \omega_i, \tag{3a}$$

$$M_i\dot{\omega}_i = P_{mi} - \sum_k \left(\frac{E_i E_k}{x_{ik}} \sin(\delta_{ik})\right) - D_i\omega_i, \tag{3b}$$

where $\omega_s = 120\pi$ (rad/sec) is the synchronous speed for the 60 Hz system, for $i = 1, \ldots, n$. Linearizing (3) about the equilibrium $(\delta_{i0}, 0)$ results in the small signal model:

$$\left[\begin{array}{c} \Delta\dot{\delta} \\ \hline \Delta\dot{\omega} \end{array}\right] = \underbrace{\left[\begin{array}{c|c} 0 & I_n \\ \hline \mathcal{M}^{-1}\mathcal{L} & -\mathcal{M}^{-1}\mathcal{D} \end{array}\right]}_{\mathcal{A}} \left[\begin{array}{c} \Delta\delta \\ \hline \Delta\omega \end{array}\right] + \underbrace{\left[\begin{array}{c} 0 \\ \hline \mathbf{e}_j \end{array}\right]}_{\mathcal{B}} u, \tag{4}$$

where, $\Delta\dot{\delta} = [\Delta\dot{\delta}_1 \cdots \Delta\dot{\delta}_n]^T$, $\Delta\dot{\omega} = [\Delta\dot{\omega}_1 \cdots \Delta\dot{\omega}_n]^T$, I_n is the n-dimensional identity matrix, $\mathbf{e}_j$ is the j^{th} unit vector with all elements zero but the j^{th} element that is 1, considering that the input is modeled as a change in the mechanical power in the j^{th} machine. However, since we are interested only in the oscillatory modes or eigenvalues of $\mathcal{A}$, this assumption is not necessary, and the input can be modeled in any other feasible way such as faults and excitation inputs. The matrix $\mathcal{L}$ in (4) is the $n \times n$ Laplacian matrix of the form:

$$\mathcal{L}_{ij} = \big(E_i E_j \cos(\delta_{i0} - \delta_{j0})\big)/x_{ij} \quad i \neq j, \tag{5a}$$

$$\mathcal{L}_{ii} = -\sum_{k=1}^{n} \big(E_i E_k \cos(\delta_{i0} - \delta_{k0})\big)/x_{ik}. \tag{5b}$$

It is obvious that $\mathcal{L}_{ij} = \mathcal{L}_{ji}$. Let us denote the i^{th} eigenvalue of the matrix $\mathcal{M}^{-1}\mathcal{L}$ by λ_i. The largest eigenvalue of this matrix is equal to 0, and all other eigenvalues are negative, i.e. $\lambda_n \leq \cdots \leq \lambda_2 < \lambda_1 = 0$. Assuming the magnitude of D_i/M_i are small, the eigenvalues of $\mathcal{A}$ can be approximated by $\pm j\Omega_i$ ($j = \sqrt{-1}$), where $\Omega_i = \sqrt{|\lambda_i|}$.

Now, assuming that the entire network consists of r coherent areas that are sparsely-connected, and the i^{th} area consists of m_i nodes with connections defined by $\mathcal{M}_i^{-1}\mathcal{L}_i$, $(i = 1, \ldots, r)$, one can then rewrite (4) as shown in:

$$\begin{bmatrix} \Delta\ddot{\delta}_1^1 \\ \vdots \\ \Delta\ddot{\delta}_{m_1}^1 \\ \hline \Delta\ddot{\delta}_1^2 \\ \vdots \\ \ddot{\delta}_{m_2}^2 \\ \hline \vdots \\ \hline \Delta\ddot{\delta}_1^r \\ \vdots \\ \Delta\ddot{\delta}_{m_r}^r \end{bmatrix} = \underbrace{\left[\begin{array}{c|c|c|c} \mathcal{M}_1^{-1}\mathcal{L}_1 + \mathcal{K}_1 & * & * & * \\ \hline * & \mathcal{M}_2^{-1}\mathcal{L}_2 + \mathcal{K}_2 & * & * \\ \hline * & * & \ddots & * \\ \hline * & * & * & \mathcal{M}_r^{-1}\mathcal{L}_r + \mathcal{K}_r \end{array}\right]}_{\mathcal{M}^{-1}\mathcal{L}} \begin{bmatrix} \Delta\delta_1^1 \\ \vdots \\ \Delta\delta_{m_1}^1 \\ \hline \Delta\delta_1^2 \\ \vdots \\ \Delta\delta_{m_2}^2 \\ \hline \vdots \\ \hline \Delta\delta_1^r \\ \vdots \\ \Delta\delta_{m_r}^r \end{bmatrix} \Rightarrow$$

$$- \mathcal{M}^{-1}\mathcal{D}\Delta\dot{\delta} + \mathbf{e}_j u \tag{5}$$

where, $\Delta\delta_j^i$ means the angle of the j^{th} machine in the i^{th} area. Construction of matrices $\mathcal{K}_i$ follows from the definitions of $\mathcal{A}$ and $\mathcal{M}_i^{-1}\mathcal{L}_i$ for $i = 1, \ldots, r$. The off-diagonal blocks of the matrix $\mathcal{M}^{-1}\mathcal{L}$ are shown by asterisks $(*)$. The $(i,j)^{th}$ off-diagonal block shows the connectivity between areas i and j in the Kron-reduced form. Due to the assumption of coherency following from the difference between the local and inter-cluster reactances and inertias, the oscillatory modes of the matrix $\mathcal{A}$ will be divided into sets of $(r-1)$ inter-area modes with eigenvalues $-\sigma_1 \pm j\Omega_1$ through $-\sigma_{r-1} \pm j\Omega_{r-1}$. The remaining $(n-r)$ modes will be characterized by intra-area modes representing the local oscillations inside areas. In fact, as shown in [16], if the inertias $M_i \ \forall \ i = 1, \ldots, n$, are of the same order of magnitude, then from (5a) it is clear that $\mathcal{L}_{ij}$ will be a large positive number for nodes i and j that are connected by a short tie-line with small reactance x_{ij} while $\mathcal{L}_{ij}$ will be a small positive number for nodes that are connected by a long transmission line with large reactance x_{ij}, leading to a sharp separation of inter-area and intra-area frequencies. Our basic assumption for dynamic equivalencing is that the $(r-1)$ inter-area modes can be attributed to r equivalent machines. Let E_k^E, $\delta_k^E(t)$, and $\omega_k^E(t) \triangleq \dot{\delta}_k^E(t)$ denote the voltage, angle, and frequency of the k^{th} equivalent machine, respectively. The equivalent small-signal model for the inter-area dynamics of (4) is shown in:

$$\begin{bmatrix} \Delta\ddot{\delta}_1^E \\ \Delta\ddot{\delta}_2^E \\ \vdots \\ \Delta\ddot{\delta}_r^E \end{bmatrix} = \underbrace{\begin{bmatrix} (\mathcal{M}_1^E)^{-1}\mathcal{L}_{11}^E & * & * & * \\ * & (\mathcal{M}_2^E)^{-1}\mathcal{L}_{22}^E & * & * \\ * & * & \ddots & * \\ * & * & * & (\mathcal{M}_r^E)^{-1}\mathcal{L}_{rr}^E \end{bmatrix}}_{(\mathcal{M}^E)^{-1}\mathcal{L}^E} \begin{bmatrix} \Delta\delta_1^E \\ \Delta\delta_2^E \\ \vdots \\ \Delta\delta_r^E \end{bmatrix}$$

$$-(\mathcal{M}^E)^{-1}\mathcal{D}^E\Delta\dot{\delta}^E + \mathbf{e}_j^E u^E \tag{6}$$

where $\Delta\delta^E \triangleq [\Delta\delta_1^E \ \dots \ \Delta\delta_1^E]^T$, and $\mathcal{M}^E$ and $\mathcal{D}^E$ are $(r \times r)$ diagonal matrices of equivalent machine inertias and equivalent machine dampings, respectively. $\mathcal{L}^E$ represents the connectivity of the r areas in the equivalent topology whose elements are as follows:

$$\mathcal{L}_{ij}^E = \big(E_i^E E_j^E \cos(\delta_{i0}^E - \delta_{j0}^E)\big)/x_{ij}^E, \quad i \neq j \tag{7a}$$

$$\mathcal{L}_{ii}^E = -\sum_{k=1}^{r} \big(E_i^E E_k^E \cos(\delta_{i0}^E - \delta_{k0}^E)\big)/x_{ik}^E, \tag{7b}$$

where, x_{ij}^E is the equivalent reactance of the tie-line connecting areas i and j in the reduced-order model.

Our objective is to find the equivalent topology that connects these r equivalent machines using PMU data, which is equivalent to estimating the elements of the matrix $\mathcal{L}^E$. Given the measurements of $\Delta\delta$ and $\Delta\omega$ from (5), our first task, therefore, is to apply modal decomposition techniques by which we can extract the slow components of these outputs, i.e., $\Delta\delta^E$ and $\Delta\omega^E \triangleq \Delta\dot{\delta}^E$ respectively, as defined in (6), and, thereafter, use these slow components to estimate $\mathcal{L}_{i,j}^E \ \forall\, i, j = 1, \dots, r$. We next review a modal decomposition technique using Hankel matrices to achieve the first task.

3 Modal Extraction using Hankel Matrices

3.1 Modal Decomposition

As discussed in the previous section, the output measurements of (5) will contain the contribution of both inter-area and intra-area modes. The first step in topology identification of the dynamic equivalent model is to find the slow component of each measurement. Several methods for such modal extraction have recently been proposed both in the power system literature [29, 30, 31, 32], and in the control systems literature [33] with applications to real-world power system models such as the WECC system [34]. All of these methods have their own advantages and disadvantages depending on applications. Among them, subspace identification methods such as Eigensystem Realization Algorithm (ERA) [32] have been shown to be very useful tools for identifying slow oscillation modes from PMU data. The choice of ERA also follows from the fact that it is computationally fast and can be implemented in real-time. We next summarize the basic ERA algorithm as follows.

Let us consider a general continuous-time LTI system:

$$\dot{\mathbf{x}}(t) = A\mathbf{x}(t) + B\mathbf{u}(t), \ \mathbf{y}(t) = C\mathbf{x}(t), \tag{8}$$

where $A \in \mathbb{R}^{n\times n}$, $B \in \mathbb{R}^{n\times p}$, and $C \in \mathbb{R}^{q\times n}$ are unknown state space matrices and need to be identified from the output measurements $\mathbf{y}(t)$ and the input $\mathbf{u}(t)$. We assume the triplet (A, B, C) are controllable and observable. Also, $\mathbf{u}(t)$ is assumed to be persistently exciting. The discrete-time equivalent of (8) is written as

$$\mathbf{x}(k+1) = A_d\mathbf{x}(k) + B_d\mathbf{u}(k), \quad \mathbf{y}(k) = C\mathbf{x}(k). \tag{9}$$

The impulse response of (9) will be

$$\mathbf{y}(k) = CA_d^{k-1}B_d. \tag{11}$$

Given measurement $\mathbf{y}(k)$ for $k = 0, \dots, m$, we next construct two $l \times s$ Hankel matrices H_0 and H_1 as:

$$H_0 \triangleq \begin{bmatrix} \mathbf{y}_0^0 & | & \mathbf{y}_1^0 & | & \cdots & | & \mathbf{y}_s^0 \end{bmatrix}, \tag{12a}$$

$$H_1 \triangleq \begin{bmatrix} \mathbf{y}_0^1 & | & \mathbf{y}_1^1 & | & \cdots & | & \mathbf{y}_s^1 \end{bmatrix}, \tag{12b}$$

where l and s are positive integers satisfying $(n < l, n < s, s+l \leq m)$, $\mathbf{y}_i^j = \text{col}(\mathbf{y}(i+j)..\mathbf{y}(i+j+l-1))$ for $j = 0, 1$ and $i = 1, \dots, s$. It can be easily shown that $H_0 = \mathcal{O}\mathcal{C}$ and $H_1 = \mathcal{O}A_d\mathcal{C}$, where $\mathcal{O}$ and $\mathcal{C}$

are observability and controllability matrices for (9), respectively. We next consider the truncated singular value decomposition of H_0 by retaining its largest n singular values as[1]

$$\hat{H}_0 = \hat{R}\ \hat{\Sigma}\ \hat{S}^T. \tag{13}$$

Defining $\mathcal{E}_1 \triangleq \begin{bmatrix} I_p & 0_{p\times(s-p)} \end{bmatrix}^T$ and $\mathcal{E}_2 \triangleq \begin{bmatrix} I_q & 0_{q\times(l-q)} \end{bmatrix}^T$, the estimates for the triplet (A_d, B_d, C) up to a similarity transformation can be calculated as

$$\hat{A}_d = \hat{\Sigma}^{-1/2}\, \hat{R}^T\, H_1\, \hat{S}\ \hat{\Sigma}^{-1/2}, \tag{14}$$

$$\hat{B}_d = \hat{\Sigma}^{1/2}\ \hat{S}^T\, \mathcal{E}_1, \quad \hat{C} = \mathcal{E}_2^T\, \hat{R}\ \hat{\Sigma}^{1/2}. \tag{11}$$

One can next convert $(\hat{A}_d, \hat{B}_d, \hat{C})$ to their continuous-time counterpart $(\hat{A}, \hat{B}, \hat{C})$ by zero-order hold. For our application, since the eigenvalues of A satisfy the two time-scale property of (5), the oscillatory components of the output response of (8) can be estimated as

$$\hat{\mathbf{y}}(t) = \underbrace{\sum_{i=1}^{r-1} (\boldsymbol{\alpha}_i \pm j\boldsymbol{\beta}_i) e^{(-\sigma_i \pm j\Omega_i)t}}_{\mathbf{y}^E(t),\ \text{inter-area modes}} + \underbrace{\sum_{k=r}^{n-1} (\boldsymbol{\alpha}_k \pm j\boldsymbol{\beta}_k) e^{(-\sigma_k \pm j\Omega_k)t}}_{\mathbf{y}^I(t),\ \text{intra-area modes}}, \tag{16}$$

where $-\sigma_i \pm j\Omega_i$ are the eigenvalues of $\hat{A}$, and the residues $\boldsymbol{\alpha}_i \pm j\boldsymbol{\beta}_i$ follow from the state-space structure of $(\hat{A}, \hat{B}, \hat{C})$ for $i = 1, \ldots, n-1$. Therefore, given PMU measurements $\mathbf{y}(t)$ one can easily construct $\mathbf{y}^E(t)$ using (8)-(16). Note that if $\mathbf{y}(t)$ is corrupted by additive white Gaussian noise, one may use the stochastic variant of ERA [35] to preserve the accuracy of estimating $\mathbf{y}^E(t)$.

It is important to note that ERA alone cannot be used for solving the topology identification problem. This is because $\hat{A}_d$ will only be a similarity transform of A_d and, therefore, may not capture the topology of the system through a Laplacian structure. Thus, we have to cast the problem using a parameter estimation framework as presented in Section 5.

Remark 1 The standard approach for doing modal decomposition, as shown in [30] is to assume the input to be an impulse function. Accordingly, in (9) we assumed $\mathbf{u}(k)$ to be an impulse input. In fact, since we are interested in identifying only the inter-area modes, even if $\mathbf{u}(k)$ is not an impulse, ERA will still give accurate results provided that its frequency content do not lie in the inter-area frequency range.

Remark 2 In literature, ERA has been shown to be robust to noise. For example, in [35], it is shown that if both the process and measurement noise are zero mean white Gaussian and the stochastic process is zero mean stationary, then there exist stochastic variants of ERA which preserves the accuracy of the estimated modes.

Remark 3 Here, we assumed a single output to describe the ERA algorithm. However, ERA algorithm can be generalized for multiple outputs as well. In our power system application, we assumed that we have at least one measurement from any area. Then, clearly the system will be observable. Also, we assume that the input $u(t)$ will persistently excites all slow modes of system, i.e., the dynamic equivalent model to be identified is both controllable and observable.

4 Description of 5-Area model

As mentioned before, the WECC system is divided into five separate areas which are connected in a linear topology through long 500 kV transmission lines following the example cited in [3]. These five

[1]Note that ERA depends on the SVD of the Hankel matrix H_0, and therefore, does not depend on the diagonalizability of A_d.

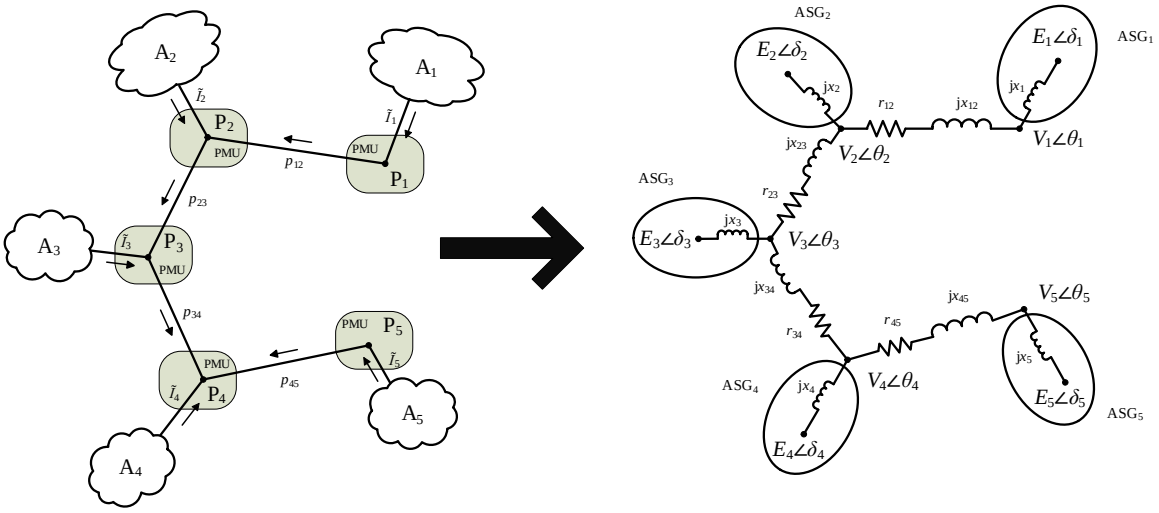

Figure 2: Electrical topology of WECC's 500kV network

areas are represented by five aggregated synchronous generators (ASG) with the interconnecting 500 kV lines between any two areas can be reduced to a single equivalent transmission line between those two areas. This reduction is shown in figure 2.

Although the equivalent transmission lines are reduced versions of real-world transmission lines, they connect five real-world sub-stations on the 500 kV network to each other cyclically. These sub-stations, referred to as pilot buses, are selected from each area based on the following criteria and are shown in figure 2:

– The sub-station must have a PMU installed at it's location

– All generators within that area lie behind this sub-station

The voltage phasor, $V_i \angle \theta_i$ is known at each pilot bus owing to availability of PMU data at that bus. Furthermore, the current $I_i \angle \alpha_i$ being injected at each pilot bus can be calculated from the difference in line currents flowing in and out of that pilot bus, which are known quantities from PMU data.

$$\tilde{I}_i = \tilde{I}_{ik} - \tilde{I}_{ji} \tag{12}$$

The pilot bus of a particular area also acts as the terminal bus for the aggregated synchronous generator which represents that area. Looking from the pilot bus into the area, this generator is modeled as a Thevenin voltage source with internal EMF $E_i \angle \delta_i$ and Thevenin reactance jx_i. Due to non-identifiability, it is not possible to model it as an impedance of $r_i + jx_i$. This is further elaborated upon in section 5.3. Each aggregated synchronous generator is modeled as a second order damped oscillator described by the swing equation (2a)-(2b). Since these ASGs are fictitious generators, their model parameters are not known, and need to be identified using PMU measurements of voltage and phase angles measured at the corresponding pilot bus. Thus, the parameter identification for the five-area model is a three step process:

– Identification of long tie line impedance $r_{ij} + jx_{ij}$

– Identification of Thevenin reactance jx_i of ASG

– Identification of inertia M_i and damping D_i of ASG

Also, as indicated in Section 3, since the ASG is obtained by collapsing coherent areas of the network, the non-coherent modes or local modes must be removed from the PMU measurements before they can be used to identify the above three quantities for each ASG. In other words, the

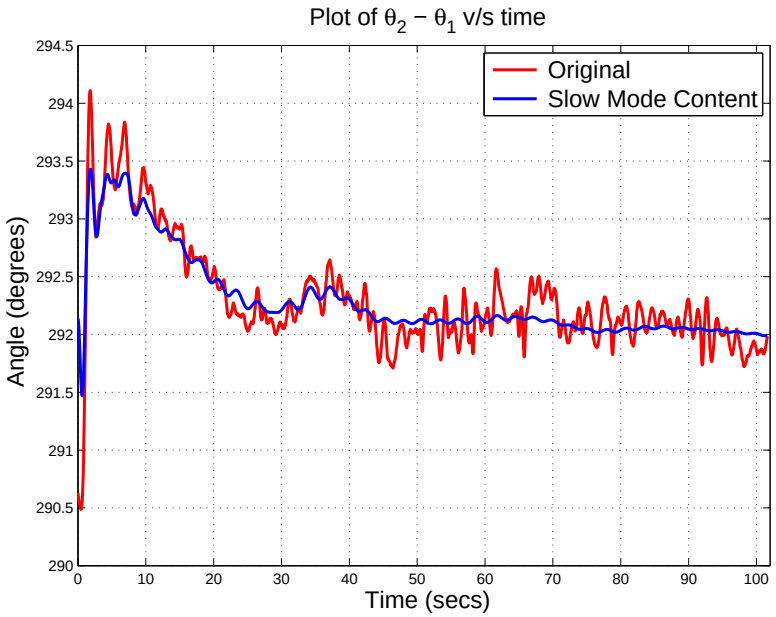

Figure 3: Slow mode component of Voltage angle difference between Station 2 and Station 1

raw PMU data contains both fast local modes as well as slow inter-area modes, and must be passed through a band-pass filter to remove the faster modes. However, since such filtering typically adds a phase shift to the slow modes, distorting the data, an alternative time-domain approach of using modal decomposition method is applied, as described in Section 3. We next briefly describe the method adopted for this particular case, namely the Prony algorithm. Prony analysis, which is a time-domain based curve fitting technique, is used to determine frequency, amplitude, phase and damping components of the 'equivalent' PMU measurement from the pilot buses. Essentially, any stream of PMU data can be formulated as

$$y(t) = x(t) + n(t) \approx n(t) + \sum_{i=1}^{M} R_i e^{\lambda_i t} \tag{13}$$

where $y(t)$ is the observed time response
$x(t)$ is the reconstructed signal
$n(t)$ is noise
R_i is the complex amplitude of i^{th} component
λ_i $= \sigma_i + j\omega_i$
$-\sigma_i$ is the damping coefficient of i^{th} component
ω_i is the angular frequency of i^{th} component

Prony's method returns a set of exponential and damped oscillatory components, which when combined create $x(t)$ that provides the best possible least-squares fit to $y(t)$. The least-squares fit is constrained by the value of M. The obtained list of components are then subject to the constraint, $\omega_i < 2\pi$ rad/s to obtain the slow modes. The voltage angle difference between pilot bus 1 and 2, and its slow mode component obtained from the Prony algorithm are shown in Figure 4. We present a detailed description of the modal extraction results for the various event dates provided to us in the Appendix. For the sake of completeness, we compare the results of the Prony algorithm with that of Matrix Pencil method. In the next section we outline the estimation process of the three essential model parameters listed above using the extracted slow mode components of the PMU measurements.

5 Model parameter estimation

5.1 Identification of inter-area tie-line impedance

The reduced-order model assumes that each station S_i is connected to the next station S_j through a single equivalent transmission line. Since this line is a reduction of several long 500 kV transmission lines, the equivalent-π model of the transmission line must be used for analysis. In order to calculate the equivalent shunt admittance at the end of each line, we require the voltage at the pilot buses and the line charging current. However, the line charging current at any bus is not available from PMU data, and hence it is not possible to estimate the equivalent shunt admittance from PMU data alone. The following two alternative approaches can be adopted:

– The shunt admittance values of a transmission line of a given length can be estimated from typical values of admittance per mile values for 500kV transmission lines for a given conductor configuration, or

– The shunt admittance of the transmission lines can be merged with the shunt load present at the ASG, thus effectively eliminating them from analysis.

To ensure that all parameters can be evaluated using PMU data alone, the second approach is adopted in this paper, and the long transmission lines are represented by pure series impedance. This series impedance can be calculated from the voltage phasors $\tilde{V}_i$ and $\tilde{V}_j$ available at the pilot buses from PMU data. Additionally, the physical 500 kV lines between the aforementioned two pilot buses are identified, and lines with substantially larger currents are selected for analysis. The net current $\tilde{I_{ij}}$ between the two pilot buses along the fictitious transmission line is taken as the phasor sum of the currents in the previously selected transmission lines. Using the voltages and currents thus obtained, the inter-tie impedance can now be calculated using Ohm's law as:

$$\tilde{V}_i - \tilde{V}_j = \tilde{I}_{ij} \cdot Z\angle\theta_z \tag{14}$$

Separating out real and imaginary parts,

$$V_i \cos\theta_i - V_j \cos\theta_j = I_{ij} Z \cos(\theta_z + \alpha) \tag{15}$$

$$V_i \sin\theta_i - V_j \sin\theta_j = I_{ij} Z \sin(\theta_z + \alpha) \tag{16}$$

Each data-point has two equations with two unknown parameters Z and θ_z. Thus the above set of equations can be solved algebraically using least squares technique for each data-point to calculate Z and θ_z.

5.2 Identification of intra-area Thevenin reactance

After the estimation of "inter-tie" impedances, the next logical step is to estimate the small "intra-tie" impedance values that connect the generator voltage source to the pilot bus. The estimation of internal voltage magnitude E_i, internal voltage angle δ_i and intra-tie impedance x_i was approached from several directions, some of which are listed below. Before describing these approaches, the assumptions made in these techniques are listed.

1. Assumption 1: E_i is assumed to be a constant magnitude

This assumption is important because for every point of data, there are two equations. Thus there are $2N_s$ equations overall. The unknowns in these equations are E_i, δ_i, r_i and x_i. If E is a varying quantity, then we will have $2N_s + 2$ variables and only $2N_s$ equations. Thus the problem is not identifiable for varying E_i. If E_i is considered as a constant but unknown parameter, the number of variables in the problem reduces to $N_s + 3$. Thus this case is theoretically identifiable for $N_s > 3$. This is true for PMU data which is usually three to five minutes long sampled at 15 to 30 samples per second, making N_s very large. It is also reasonable to take E_i constant since the second order model for the generator is used for analysis. Field dynamics are ignored due to the absence of field currents and voltages for the ASG.

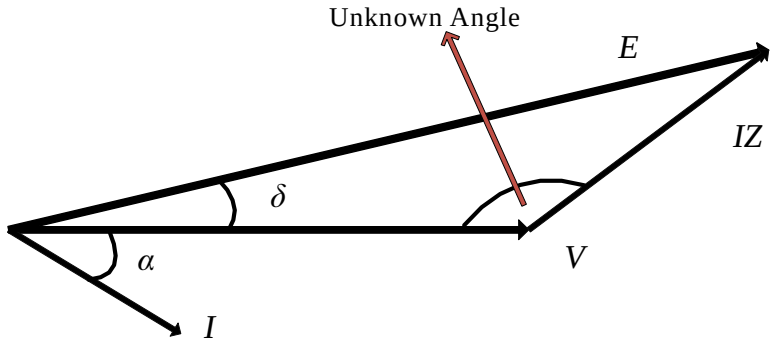

Figure 4: Phasor Diagram for the Aggregated Synchronous Generator

5.3 Problem of non-identifiability

From the figure below, it is clear that the phasors E, V and IZ form a triangle. The angles, δ and α are marked in the figure.

Thus, in this triangle sine rule can be written as follows:

$$\frac{a}{\sin A} = \frac{b}{\sin B} = \frac{c}{\sin C} \tag{17}$$

Here, a, b and c are the lengths of the sides opposite to the vertices A, B and C respectively. Thus:

$$a = l(BC),\ b = l(AC),\ c = l(AB) \tag{18}$$

For the triangle above:

$$\frac{E}{\sin(\theta_z + \alpha)} = \frac{IZ}{\sin\delta} = \frac{V}{\sin(180^\circ - \theta_z - \alpha - \delta)} \tag{19}$$

The above set of equations cannot be solved for unique values of E, Z and θ_z. This is because none of the ratios are known and the sides of the triangle E and IZ cannot be uniquely determined. Another way to look at this is as follows. Both E and IZ are unknown. V is known, but E and IZ both can take an infinite pair of values so that they satisfy $V = EIZ$. Hence, to make the system identifiable, the following assumptions are made:

– $E_i = 1$ per unit, and

– $r_i = 0$, or $\theta_z = 90^\circ$, or $Z_i = jx_i$.

Using the above two assumptions, equation (1.11) reduces to:

$$\frac{1}{\sin(90^\circ + \alpha_i)} = \frac{I_i x_i}{\sin\delta_i} = \frac{V_i}{\sin(90^\circ - \alpha_i - \delta_i)} \tag{20}$$

or,

$$\frac{1}{\cos\alpha_i} = \frac{I_i x_i}{\sin\delta_i} = \frac{V}{\cos(\alpha_i + \delta_i)} \tag{21}$$

From the above equation, the following two equations can be written:

$$\delta_i = \cos^{-1}(V_i \cos\alpha_i) - \alpha_i \tag{22}$$

$$x_i = \frac{\sin\delta_i}{I_i \cos\alpha_i} \tag{23}$$

Thus, the system is identifiable in the light of these two assumptions. It may be noted that these are all algebraic relationships and x_i and δ_i can be calculated for each and every data point.

5.4 Identification of Equivalent Inertia and Damping

After the estimation of the inter-tie and intra-tie reactance values for the five-machine aggregated synchronous generator equivalent network for the WECC system, estimation of M_i and D_i from PMU data and reactance values is the next step. To estimate M_i and D_i for each ASG, filtered PMU data from the pilot buses as well as the reactance values estimated in the previous steps are used. For the i^{th} generator ASG_i, the sma–signal electro-mechanical dynamics using the models of Section 2 can be represented by

$$\begin{bmatrix} \Delta\dot{\delta}_i \\ \Delta\dot{\omega}_i \end{bmatrix} = \begin{bmatrix} \omega_s\Delta\omega_i \\ \frac{-2D_i}{M_i}\Delta\omega_i - \frac{1}{M_i}\Delta P_{ei} + \frac{1}{M_i}\Delta P_{mi} \end{bmatrix} \tag{24}$$

Using the expression for P_{ei} as

$$P_{ei} = \frac{E_i V_i}{x_i}\sin(\delta_i - \theta_i) \tag{25}$$

and linearizing we obtain,

$$\Delta P_{ei} = \frac{E_i}{x_i}\sin(\delta_{i0} - \theta_{i0})\Delta V_i + \frac{E_i V_i}{x_i}\cos(\delta_{i0} - \theta_{i0})(\Delta\delta_i - \Delta\theta_i) \tag{26}$$

Moreover, $\vec{I} = \bar{Y}_{bus}\vec{V}$ can be written using Kirchoff's Current law. But for the generators, from Kirchoff's Voltage law, $\vec{I} = \bar{Y}_g(\vec{E} - \vec{V})$, where $\bar{Y}_g = diag(1/jx_i)$. Combining these equations, we get $\vec{V} = \bar{Y}\vec{E}$, where $\bar{Y} = (\bar{Y}_{bus} + \bar{Y}_g)^{-1}\bar{Y}_g$. Separating out real and imaginary parts,

$$V_R = V_i\cos\theta_i = Y_R E_i\cos\delta_i - Y_I E_i\sin\delta_i \tag{27}$$

$$V_I = V_i\sin\theta_i = Y_I E_i\cos\delta_i + Y_R E_i\sin\delta_i \tag{28}$$

Linearizing,

$$\Delta V_R = \cos\theta_{i0}\Delta V_i + V_{i0}\sin\theta_{i0}\Delta\theta = (-Y_R E_i\sin\delta_{i0} - Y_I E_i\cos\delta_{i0})\Delta\delta_i \tag{29}$$

$$\Delta V_I = \sin\theta_{i0}\Delta V_i + V_{i0}\cos\theta_{i0}\Delta\theta = (-Y_I E_i\sin\delta_{i0} + Y_R E_i\cos\delta_{i0})\Delta\delta_i \tag{30}$$

Through mathematical manipulation of (29) and (30), the following result is obtained:

$$\begin{bmatrix} \Delta V \\ \Delta\theta \end{bmatrix} = \begin{bmatrix} F & 0_{5X5} \\ G & 0_{5X5} \end{bmatrix}\begin{bmatrix} \Delta\delta \\ \Delta\omega \end{bmatrix} \tag{31}$$

where

$$\begin{bmatrix} F \\ G \end{bmatrix} = \begin{bmatrix} diag(\cos\theta_{i0}) & -diag(V_{i0}\sin\theta_{i0}) \\ diag(\sin\theta_{i0}) & -diag(V_{i0}\cos\theta_{i0}) \end{bmatrix}^{-1} X \begin{bmatrix} -Y_R diag(E_i\sin\delta_{i0}) & -Y_I diag(E_i\cos\delta_{i0}) \\ Y_R diag(E_i\cos\delta_{i0}) & -Y_I diag(E_i\sin\delta_{i0}) \end{bmatrix} \tag{32}$$

Substituting (31) in (26), ΔP_{ei} can be expressed purely as a function of $\Delta\delta$ as follows,

$$\Delta P_{ei} = L_i\Delta\delta \tag{33}$$

Substituting 33 in 24, the following result is derived:

$$\begin{bmatrix} \Delta\dot{\delta}_i \\ \Delta\dot{\omega}_i \end{bmatrix} = \begin{bmatrix} \omega_s\Delta\omega_i \\ \frac{-2D_i}{M_i}\Delta\omega_i - \frac{1}{M_i}L_i\Delta\delta_i + \frac{1}{M_i}\Delta P_{mi} \end{bmatrix} \tag{34}$$

The above equation can be written in a generalized form for all five aggregated synchronous generators as follows:

$$\begin{bmatrix} \Delta\dot{\delta} \\ \Delta\dot{\omega} \end{bmatrix} = \begin{bmatrix} 0_{5X5} & \omega_s I_{5X5} \\ diag\left(\frac{-1}{M_i}\right)L & diag\left(\frac{-2D_i}{M_i}\right) \end{bmatrix}\begin{bmatrix} \Delta\delta \\ \Delta\omega \end{bmatrix} + \begin{bmatrix} 0_{5X5} \\ diag\left(\frac{1}{M_i}\right) \end{bmatrix}\Delta P_m \tag{35}$$

It can be seen that (35) and (31) are of the form

$$\dot{X} = AX + BU \tag{36}$$

$$Y = CX \tag{37}$$

where matrices A and B are unknown and are parameterized by M_i and D_i. C is known as the network structure and parameters are known from 5.1 and 5.3. Therefore, to formulate the least squares problem, M_i, D_i and P_{mi} are given arbitrary initial values within certain upper and lower bounds, and the resulting matrices $\hat{A}$ and $\hat{B}$ are calculated. These matrices are used to calculate $\hat{X}(t)$, an estimate for X by solving the differential equation 36 for step change in $u(t)$. The computed value of $\hat{X}(t)$ is then used to calculate an estimate of Y using $\hat{Y}(t) = C\hat{X}(t)$. The least squares problem is finally formulated as the optimal solution of M_i, D_i and P_{mi} obtained by minimizing the integral

$$\int_{t=0}^{t^*} \|Y(t) - \hat{Y}(t)\|_2^2 dt \tag{38}$$

where $Y(t)$ is obtained from PMU measurements. For the purpose of simulation, $Y(t)$ was restricted only to $\Delta\theta(t)$ to reduce computational burden.

Line	Reactance
Station 1-Station 2	56.34 + 120.39j
Station 2-Station 3	0.64 + 22.67j
Station 3-Station 4	30.83 + 81.16j
Station 4-Station 5	11.03 + 94.51j

Table 1: Calculated inter-tie impedance values

Machine	Tie-line Reactance	
	Calculated	Used
Station 1	24.8986j	24.8986j
Station 2	18.1871j	18.1871j
Station 3	-3.4j	18.7462j
Station 4	18.7462j	18.7462j
Station 5	34.4729j	34.4729j

Table 2: Calculated intra-tie impedance values

6 Model Validation

After identification of the model parameters, the next step is to validate these parameters by further tuning them until and unless the predicted phase angle responses of the estimated model closely matches the inter-area component of the angles obtained from the measured PMU data. For the purpose of implementation in a real-time digital simulator, several other model parameters also need to be used. These parameters include load resistances, governor power set points, internal machine voltage references, machine inertia, machine damping, and various reactance values in the model. Table 3 gives an overview of all the final values used in the model. In this section we will explain in details how these values were calculated, tuned, and altered in order to allow the model to as closely represent the real-world system as possible.

6.1 Station 3 Tie-line Impedance Negative

The least squares calculations produced a negative tie-line impedance at Station 3, as can be seen in Table 2. This is because of the existence of a large capacitor bank at this point in the real

Machine	Station 1	Station 2	Station 3	Station 4	Station 5
Inertia MWs/MVA	75	162.92	244.636	32.42	24.82
Damping (D)	10	15	3.688	0.594	0.621
Rated MVA	1500	2500	3000	3000	3000
Machine Internal Voltage	0.993 pu	0.967 pu	0.995 pu	0.995 pu	1.021 pu
Bus Load Prefault MW	0	679	3000	2791	1000
Bus Load Postfault MW	0	0	3000	2000	2216
Pre-Fault Gov. Load Ref.	0.4464 pu	0.8293 pu	0.5591 pu	0.6264 pu	0.5476 pu
Post-Fault Gov. Load Ref.	0.4689 pu	0.8272 pu	0.5046 pu	0.6505 pu	0.5685 pu
Tie Line Z	24.8986j	18.1871j	18.7462j	18.7462j	34.4729j
Exciter Model (IEEE)	Type ST1	Type ST1	Type ST1	Type ST1	Type ST1
Governor model	Type 1	Type 1	Type 1	Type 1	Type 1
Bus Type	PQ	PQ	Slack	PQ	PQ

Table 3: Model parameters used for RTDS implementation

Bus	Voltage	
	Simulated	Real Data
Station 1	1.005 pu	0.996 pu
Station 2	0.985 pu	0.963 pu
Station 3	1.027 pu	1.006 pu
Station 4	0.974 pu	0.977 pu
Station 5	0.966 pu	0.982 pu

Table 4: Bus Voltages

WECC system that helps to sustain the voltage at this bus. The least squares calculations do not account for the presence of capacitors, but merely try and calculate inter and intra-area tie-line values to minimize the error integral in (38). Station 3 is a very heavy load bus representing the San Francisco metropolitan area. Without a capacitor placed on this bus, the voltage would sag to unacceptably low levels. This was seen in the RSCAD model as well. Without considering negative tie-line impedance, the voltage at Station 3 was drooping very low in the model. The addition of a capacitor to the model allowed the voltage to become a more acceptable level while also better representing the real-world setting. The value of this capacitor was chosen such that the voltage on this bus remained in a reasonable range.

6.2 Voltage Tuning

Though the phase angles are of primary interest for matching, matching the voltages to a reasonable level is important as well. The voltages were matched during the load-flow calculations computed in RSCAD. Internal voltages on the buses inside the five machines were tuned so that load-flow compilation yielded a close match on bus voltage value. The voltages were matched to the last point of data immediately prior to the fault time in the set of PMU data received. Values were matched by repeated changing of voltage set points and recompilation of the draft. The voltages, however, did not match quite as well during run-time when the model was actually running. Table 4 lists the voltages viewed in run-time versus the voltages seen in the PMU data. The values are close, lying within two percent of the actual PMU data values, which was deemed to be close enough for the model's purpose. Further retuning of the internal bus voltages to match run-time values rather than load-flow values is also possible, but was not pursued for the sake of simplicity.

6.3 Fault Power Flow Matching via Resistive Load Swapping

Observing the plots in Figure 5 one can see that at the instant of the fault i.e., at $t = 1.5$ seconds, the filtered PMU data demonstrates a sudden increase or decrease in phase angle. The actual

Line	Angle			Power Flow in MW		
	Pre-Fault	Immediate Post-fault	Difference	Pre-Fault	Post-fault	Change
Station 1-Station 2	17.45°	17.49°	0.04°	669	670.5	1.5
Station 2-Station 3	8.43°	11.15°	2.72°	1916	2595	679
Station 3-Station 4	-4.02°	-10.98°	-6.96°	-247	-672	-425
Station 4-Station 5	12.38°	-11.17°	-23.6°	639	-577	-1216

Table 5: Voltage angle and Power flow change across major tie-lines

Line	Pre-fault Angle		Post-fault Angle	
	Simulated	Real Data	Simulated	Real Data
Station 1-Station 2	17.45°	17.45°	17.50°	17.49°
Station 2-Station 3	8.42°	8.43°	11.14°	11.15°
Station 3-Station 4	-4.06°	-4.02°	-10.97°	-10.98°
Station 4-Station 5	12.37°	12.38°	-11.14°	-11.17°

Table 6: Voltage angle simulated v/s real values

values of these changes are shown in table 5. Three of the four phase angles in the filtered PMU data display a large change in angle in the immediate time of the fault. Using (25) in combination with the knowledge of the bus voltages and inter-area line reactances, it was possible to calculate the change in power necessary to recreate these instantaneous phase angle changes. The calculated change in power flow is shown in table 5, and was modeled as the addition or subtraction of resistive loads on appropriate buses in the system.

6.4 Phase Angle Tuning via Governors

Simply swapping out resistive loads, as described in the previous section, was not enough to match pre and post-fault phase angles of the model up against the steady-state values of the PMU data collected from the real-world system. The pre and post fault steady-state phase angles were further tuned using the governor load reference set points during the RTDS run-time of the model. The governors of the machines allow changing the load reference set point of the machines during run-time. This allowed the exact tuning of the phase angle steady state values during run-time both pre and post-fault by tuning the power set-points of these machines both pre and post-fault. The model values of the steady-state phase angles pre and post-fault are compared against the PMU data in table 6. Essentially, the machines have different power set-points post-fault than they do pre-fault, and this change in power set-point has allowed very close matching of the steady-state phase angles. The exact values used for these governor load reference set points are shown in table 3. The reasoning behind separating the swapping of resistors to model the instantaneous power changes across the lines and the changing of power set points in the governor is because changing the governor set point changes the phase angles across the lines on a much slower time scale than changing the immediate load at each bus. In order to recreate both the large, quick changes in phase angles of several degrees that occurs the instant the fault occurs as well as the gradual approach of the phase angles to a steady-state value, both of these methods were implemented together.

6.5 Inertias and Damping Values

As described in Section 5, the original inertia and damping values were calculated using a least squares method to match the filtered PMU data. This method alone, however, yielded a poor result. The original inertia of Station 1 is extremely small. It is also very under-damped, reflecting a low calculated damping coefficient. The calculated inertia and damping of the machines is shown below in table 7. The inertia and damping of Station 1 was altered such that the new transient response better matched the transient response of the filtered PMU data. Various values were attempted and gauged by how well the integration of the original dataset compared with that of the model

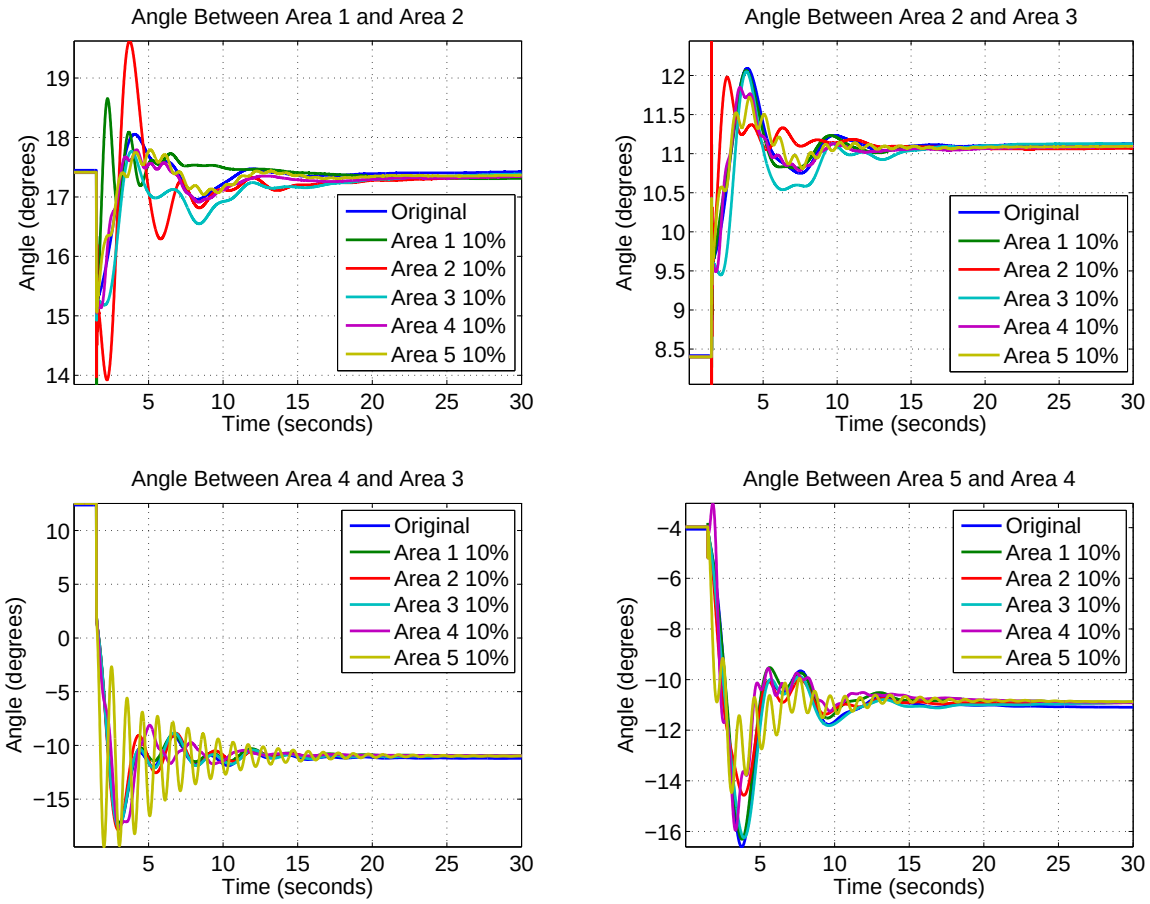

Figure 5: Model tuning for validation of phase angle at pilot buses with real PMU data

dataset. The model response with Station 1 demonstrating changes in inertia and damping are compared against the filtered PMU data. The inertia of Station 1 was also deliberately altered such that the first major peak in phase angle occurred at the same time. Observing the plots in Figure 5, one can see the response between Station 1 and Station 2 has been significantly improved while the other three transient responses remain almost identical to the model response prior to changing the inertia and damping of Station 1.

7 Sensitivity Analysis

In order to test the model, a set of contingencies are simulated to observe oscillations and analyze them to validate the model. These include

– Generator tripping resulting in loss of generation and inertia

– Line tripping resulting in increase in intra-area reactance.

Machine	Inertia		Damping	
	Calculated	Model	Calculated	Model
Station 1	1.257	75	4.776	10
Station 2	162.920	162.920	15	15
Station 3	244.636	244.636	3.688	3.688
Station 4	32.420	32.420	0.594	0.594
Station 5	24.82	24.82	0.621	0.621

Table 7: Inertia and Damping

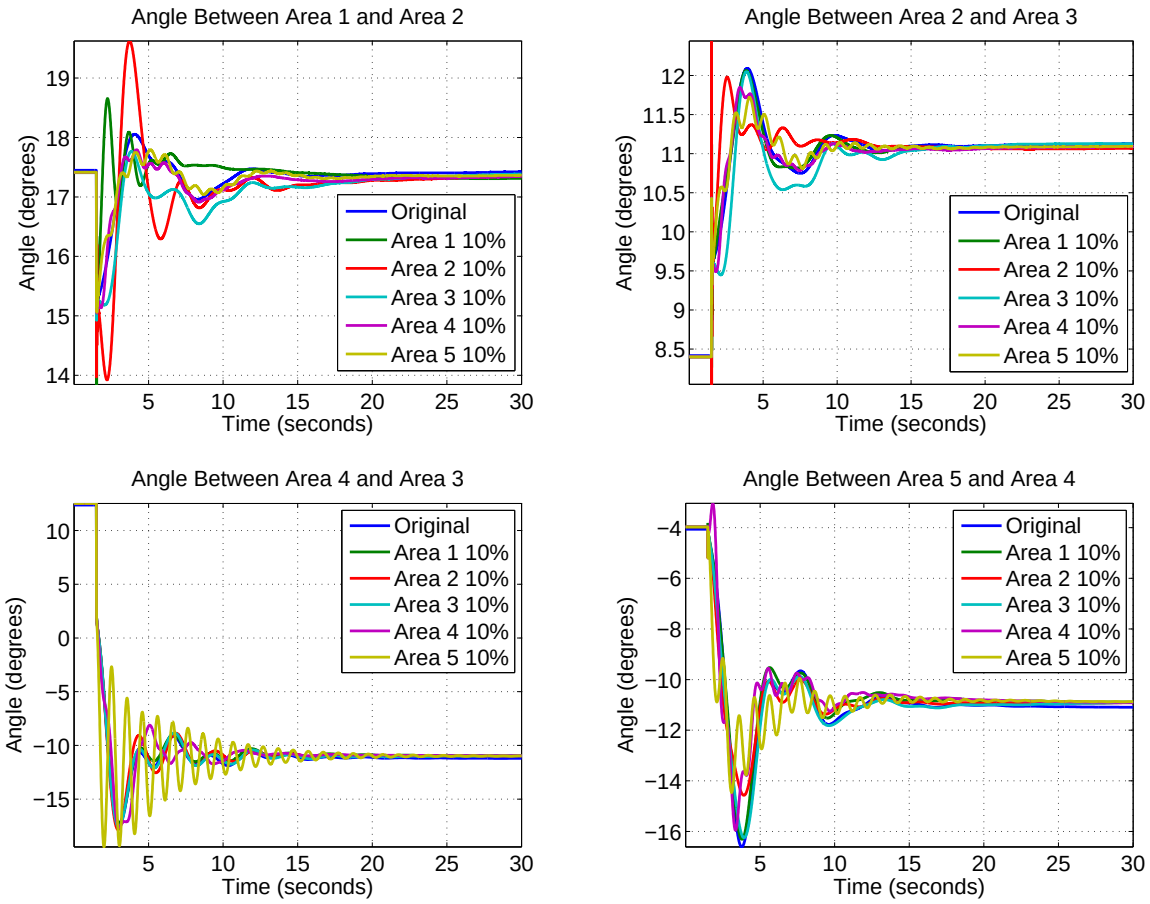

Figure 6: Contingency analysis of 5-area WECC model for loss of inertia

7.1 Contingencies

There are three sets of contingencies that have been done on the model thus far. The first set of contingencies involved the case where ten percent of the mass was lost at each bus. A separate case was ran for each machine losing ten percent inertia. The simulated loss of 1300 MW of generation at Station 5 was run and the phase angles on all four inter-area lines recorded. The results are shown below in Figure 6. It can be seen that changing the inertia by a small amount has little effect on the model's transients and no effect on the steady-state values of the model. Next, the intra-area tie-line impedance of each machine was individually increased by integer multiples of itself until instability in the model occurred. The last point before instability was used as the new value for intra-area impedance, concealed inside the machines step-up transformer. These values ended up being larger for some machines than others. Station 1 was able to be increased by a factor of ten before instability, whereas merely doubling the intra-area impedance at Station 5 caused model instability. These plots are in Figure 7. Notice that in every case there is one phase angle that is almost completely undamped. This is where the instability would start when the intra-area impedance is increased by a small amount for any generator.

7.2 Effect of faults on internal reactance

Besides simply predicting the inter-area responses of the phase angles and voltages at every pilot bus, another important aspect of the identified 5-area model is that it can help a regional transmission operator to prepare for the worst-case contingency happening in any other other. To discuss this in more details, in this section we derive the effect of faults on the internal reactance of any ASG since in the previous section we saw how the internal reactance plays a critical role in determining the stability. The effect of generator trips on the internal reactance is straight-forward as

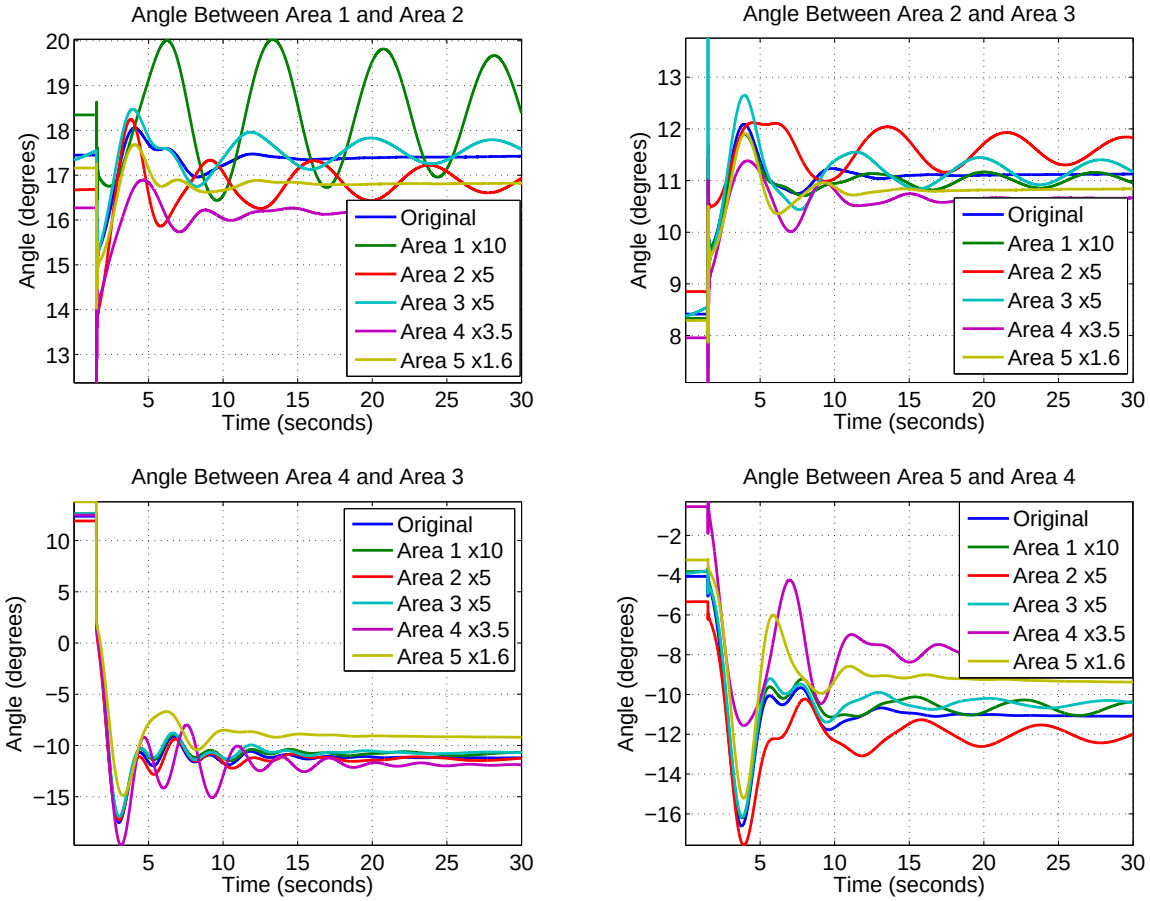

Figure 7: Contingency analysis of 5-area WECC model for local line trips

they result in a direct loss of generation and loss of inertia, and are hence modeled accordingly. Line trips, however can be modeled as an increase in intra-area reactance. For any area S_i with N_i buses, the equivalent admittance matrix Y_{bus_i} is known to the operator of that given area, along with the admittance matrix Y_{ro} for the reduced order WECC network. Also it is assumed that the operator has knowledge of the pre-disturbance power flow of area S_i as well as the power flow of the reduced order WECC model. Now, if a fault occurs within S_i, the current within the faulted line increases for a very short time and the line's protection system removes the line from the network. Let Y'_{bus_i} be the modified admittance matrix of the network after the line is removed. The admittance matrices of S_i and WECC's reduced order model are combined as follows:

$$Y_{c_i} = \begin{bmatrix} Y'_{bus_i} & Y_{cp} \\ Y_{cp}^T & Y_{ro} \end{bmatrix} \tag{39}$$

where Y_{cp} represents the coupling inter-tie admittance between pilot bus of S_i and the other pilot buses, and is a relatively sparse matrix. The resultant network has $N_i + 4$ buses, making Y_{bus_c} a square matrix of size $N_i + 4$. Assuming that the internal set-points of the generators do not change significantly due to this line loss, the power flow at PV or PQ bus j within WECC's reduced-order network is given as,

$$P_j = Re\left[\tilde{V_j} \cdot \sum_{k=1}^{N_i+4} Y_{c_i}(j,k) \cdot \tilde{V_k}\right] \tag{40}$$

$$Q_j = -Im\left[\tilde{V_j} \cdot \sum_{k=1}^{N_i+4} Y_{c_i}(j,k) \cdot \tilde{V_k}\right] \tag{41}$$

Upon using Newton-Raphson method to iteratively solve the above mentioned power flow equations at all PV and PQ buses, the updated value of $V_j \angle \theta_j$ for the j^{th} bus can be obtained. The updated

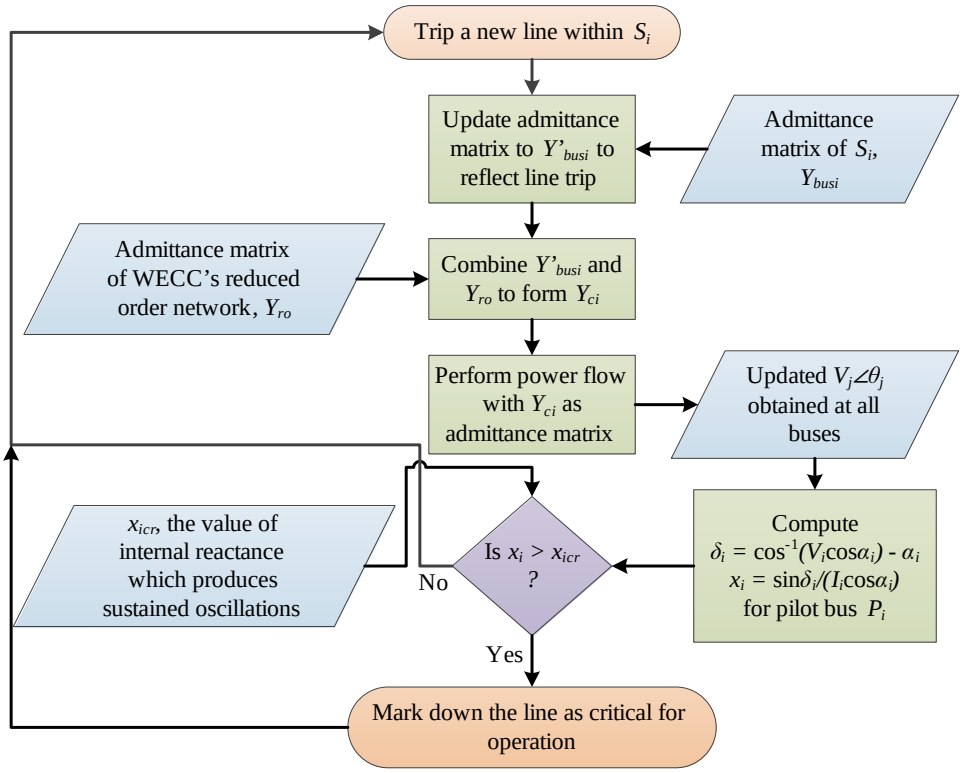

Figure 8: Algorithm for determining post-fault stability

value of the voltage phasor, thus obtained at the pilot bus of area S_i, can now be used to estimate the new value of x_i using equations (22) and (23). Although it is not apparent from the above equations, loss of a line invariably results in an increase in internal system reactance. This is due to dual effect of losing a line which directly influences x_i; and the increased power flow along unaffected lines, which increases the apparent magnitude of x_i due to infeed effects.

Algorithm 1 Determine criticality of a line within area S_i

1: **Input:** Y_{bus_i}, Admittance Matrix of area S_i
2: **Trip** a new line within S_i
3: **Update** Y_{bus_i} to Y'_{bus_i} to reflect the loss of line
4: **Input:** Y_{ro}, Admittance Matrix of WECC's reduced order network
5: **Combine** Y'_{bus_i} with Y_{ro} to form Y_{c_i}
6: **Compute** Power flow with pre-fault values for generation and loads at all buses and Y_{c_i} as the admittance matrix
7: **Update** $V_j\angle\theta_j$ at all buses
8: **Compute** x_i using 22 and 23 for pilot bus P_i
9: **Input:** $x_{i_{cr}}$, the value of internal reactance which produces sustained oscillations
10: **if** $x_i > x_{i_{cr}}$ **then**
11: **Mark** the line as critical for operation
12: **end if**
13: **Goto** Step 2

The operator can perform this analysis for several scenarios using algorithm 1 which modify the admittance matrix in different ways. Each scenario will produce a value of x_i which can be compared against a critical value of x_i for that area, which, when achieved, will cause an unacceptable amount of oscillations within that given area. The critical value for x_i can be obtained be simulating the reduced order model of WECC for incremental values of x_i and observing the point at which sustained oscillations are observed.

8 Conclusions

In this report, we developed identification techniques for dynamic equivalent model identification of the WECC power system divided into five equivalent operating areas using Synchrophasor measurements. We showed that by extracting the slow oscillatory components of a measured PMU signal, we can identify the equivalent topology of the 5-area network under assumptions on system connectivity and observability. The need for constructing the reduced-order network topology is not only to make decisions on specific lines and generators but also to create "monitoring metrics" that can be used for wide-area monitoring. For example, in [27] it was shown how PMU measurements can be used to construct inter-area energy functions for transient stability monitoring. The model in [27], however, was restricted to only two areas connected by a radial topology, and hence, there was no need to estimate the topology. The work done in this paper is a useful extension by which such energy functions can be estimated for any multi-area power systems connected by any arbitrary topology. One future direction of research will be to extend these optimization algorithms to cases when the operators have measurements only from their neighboring areas resulting in partial observability, as well as to test the model responses for inter-area oscillations when there is significant penetration of wind power at the pilot buses of WECC.

References

[1] A. G. Phadke and J. S. Thorp, *Synchronized Phasor Measurements and Their Applications.* New York, Springer, 2008.

[2] A. G. Phadke, J. S. Thorp, and M. G. Adamiak, "New Measurement Techniques for Tracking Voltage Phasors, Local System Frequency, and Rate of Change of Frequency," *IEEE Transactions on Power Apparatus and Systems*, vol. 102, pp. 1025-1038, May 1983.

[3] J. Ballance, B. Bhargava, and G. D. Rodriguez, "Use of Synchronized Phasor Measurement System for Enhancing AC-DC Power System Transmission Reliability and Capability," *Eastern Interconnection Phasor Project (EIPP) Meeting*, Sep. 2004 (available online at: http://phasors.pnl.gov/eipp_meetings.html)

[4] R. L. Cresap and J. F. Hauer, "Emergence of a New Swing Mode in the Western Power System," *IEEE Transactions on Power Apparatus and Systems*, vol. PAS-100, no. 4, pp. 2037-2045, Apr. 1981.

[5] N. Zhou, J. W. Pierre, and J. F. Hauer, "Initial Results in Power System Identification From Injected Probing Signals Using a Subspace Method," *IEEE Transactions on Power Systems*, vol. 21, no. 3, pp. 1296-1302, Aug. 2006

[6] W. A. Mittelstadt, P. E. Krause, P. N. Overholt, D. J. Sobajic, J. F. Hauer, R. E. Wilson, and D. T. Rizy , "The DOE Wide Area Measurement System (WAMS) Project Demonstration of Dynamic Information Technology for the Future Power System," *EPRI Conference on the Future of Power Delivery*, Washington, D.C., Apr. 1996.

[7] North American Synchrophasor Initiative (NASPI) - *www.naspi.org*

[8] Final Report on the August 14, 2003 Blackout in the United States and Canada: Causes and Recommendations, *Report of the U.S Department of Energy*, 2004 (https://reports.energy.gov/B-F-Web-Part1.pdf)

[9] J. Giri, M. Parashar, J. Trehern, and V. Madani, "The Situation Room: Control Center Analytics for Enhanced Situational Awareness," *IEEE Power and Energy Magazine*, vol. 10(5), pp. 24–39, 2012.

[10] G. Liu, J. Ning, Z. Tashman, V. M. Venkatasubramanian, and P. Trachian, "Oscillation Monitoring System using Synchrophasors," *IEEE PES General Meeting*, San Diego, 2012.

[11] Y. Liu, "A US-Wide Power Systems Frequency Monitoring Network," , *IEEE Power Systems Conference and Exposition*, Atlanta, GA, 2006.

[12] W. W. Price, G. E. Boukarim, J. H. Chow, R. Galarza, A. W. Hargrave, B. J. Hurysz, and R. Tapia, *Improved Dynamic Equivalencing Software,* Final Report, EPRI Project RP2447-02, 1995.

[13] R. Podmore, "A Comprehensive Program for Computing Coherency-based Dynamic Equivalents," *Proceedings of the Power Industry Computer Applications Conference* (PICA), pp. 298-306, 1976.

[14] A. Chakrabortty, J. H. Chow, and A. Salazar, "Interarea Model Estimation for Radial Power System Transfer Paths with Intermediate Voltage Control using Synchronized Phasor Measurements," *IEEE Transactions on Power Systems*, vol. 24, no. 3, pp. 1318-1326, Aug. 2009.

[15] A. Chakrabortty, J. H. Chow, and A. Salazar, "A Measurement-Based Framework for Dynamic Equivalencing of Large Power Systems Using Wide-Area Phasor Measurements," *IEEE Transactions on Smart Grid*, vol. 2(1), pp. 68–81, 2011.

[16] J. H. Chow, G. Peponides, P. V. Kokotovic, B. Avramovic, and J. R. Winkelman, *Time-Scale Modeling of Dynamic Networks with Applications to Power Systems,* Springer-Verlag, New York, 1982.

[17] R. Podmore, "Identification of Coherent Generators for Dynamic Equivalents," *IEEE Transactions on Power Apparatus and Systems*, vol. 97(4), pp. 1344–1354, 1978.

[18] R. Nath, S. S. Lamba, and K. S. Prakasa Rao, "Coherency Based System Decomposition into Study and External Areas Using Weak Coupling," *IEEE Transactions on Power Apparatus and Systems*, vol. 104(6), pp. 1443–1449, 1985.

[19] A. Chakrabortty and A. Salazar, "Building a Dynamic Electro-mechanical Model for the Pacific AC Intertie using Distributed Synchrophasor Measurements," *European Transactions on Electric Power: Special Issue on PMU Applications,* (Editors: C. C. Liu, M. Crow, J. H. Chow), vol. 21(4), pp. 1657–1672, 2011.

[20] L. Wang, M. Klein, S. Yirga, and P. Kundur, "Dynamic Reduction of Large Power Systems for Stability Studies," *IEEE Transactions on Power Systems*, vol. 12, no. 2, pp. 889-895, May 1997.

[21] G. N. Ramaswamy, L. Rouco, O. Fillatre, G. C. Verghese, P. Panciatici, B. C. Lesieutre, and D. Peltier, "Synchronic Modal Equivalencing (SME) for Structure-Preserving Dynamic Equivalents," *IEEE Transactions on Power Systems*, vol. 11(1), pp. 19–29, 1996.

[22] J. Cai, M. Furer, and N. Immerman, "An Optimal Lower Bound on the Number of Variables for Graph Identification," *Combinatorica*, vol. 12(4), pp. 389–410, 1992.

[23] M. Nabi-Abdolyousefi and M. Mesbahi, "Network Identification via Node Knock-out," *IEEE Conference on Decision and Control*, pp. 2239–2244, Atlanta, GA, Dec. 2010.

[24] G. Chowdhary, M. Egerstedt, and E. N. Johnson, "Network Discovery: An Estimation Based Approach," *American Control Conference*, pp. 1076–1081, San Francisco, CA, Jun. 2011.

[25] B. M. Sanandaji, T. L. Vincent, and M. B. Wakin, "Exact Topology Identification of Large-Scale Interconnected Dynamical Systems from Compressive Observations," *American Control Conference* pp. 649–656, San Francisco, CA, Jun. 2011.

[26] K. M. Rogers, R. D. Spadoni, and T. J. Overbye, "Identification of Power System Topology from Synchrophasor Data," *IEEE Power System Conference and Exposition*, Phoenix, AZ, 2011.

[27] J. H. Chow, A. Chakrabortty, M. Arcak, B. Bhargava, and A. Salazar, "Synchronized Phasor Data Based Energy Function Analysis of Dominant Power Transfer Paths in Large Power Systems," *IEEE Transactions on Power Systems*, vol. 22(2), 2007.

[28] A. Fouad and M. Anderson, *Power System Control and Stability,* IEEE Press; 2003.

[29] N. Zhou, J. W. Pierre, and J. F. Hauer, "Initial Results in Power System Identification From Injected Probing Signals Using a Subspace Method," *IEEE Transactions on Power Systems*, vol. 21(3), pp. 1296–1302, Aug. 2006.

[30] G. Liu, J. Quintero, and V. Venkatasubramanian, "Oscillation Monitoring System Based on Wide Area Synchrophasors in Power Systems," *Bulk Power System Dynamics and Control, iREP Symposium - iREP*, 2007.

[31] A. R. Messina, V. Vittal, D. Ruiz-Vega, and G. Enriquez-Harper, "Interpretation and Visualization of Wide-area PMU measurements using Hilbert Analysis," *IEEE Transactions Power Systems*, vol. 21(4), pp. 1760–1771, 2006.

[32] J. J. Sanchez-Gasca and J. H. Chow, "Performance Comparison of Three Identification Methods for the Analysis of Electromechanical Oscillations," *IEEE Transactions on Power Systems*, vol. 14(3), pp. 995–1002, 1999.

[33] V. M. Preciado and A. Jadbabaie, "Moment-Based Spectral Analysis of Large-Scale Networks Using Local Structural Information," *IEEE/ACM Transactions on Networking*, vol. 21(2), pp. 373–382, 2013.

[34] D. P. Chassin, Z. Huang, M. K. Donnelly, C. Hassler, E. Ramirez, and C. Ray, "Estimation of WECC System Inertia Using Observed Frequency Transients," *IEEE Transactions on Power Systems*, vol. 20(2), pp. 1190–1192, May 2005.

[35] P. Van Overschee and B. De Moor, "Subspace Algorithms for the Stochastic Identification Problem," *Proceedings of the* 30^{th} *IEEE Conference on Decision and Control*, pp. 1321–1326, vol. 2, 1991.

[36] B. Pal and B. Chaudhuri, *Robust Control in Power System,* Springer, USA, 2005.

[37] CVX Research, Inc. CVX: Matlab software for disciplined convex programming, version 2.0. http://cvxr.com/cvx, April 2011.

[38] A. Björck, *Numerical Methods for Least Squares Problems,* SIAM, Philadelphia, 1996.

[39] T. Athay, R. Podmore, and S. Virmani, "A Practical Method for the Direct Analysis of Transient Stability," *IEEE Transactions on Power Apparatus and Systems*, vol. 98(2), pp. 573–584, 1979.

[40] M. Gibbard and D. Vowles, *Simplified 14-Generator Model of the SE Australian Power System*, The University of Adelaide, Adelaide, South Australia, 2007.

[41] L. Ljung, *System Identification*, John Wiley & Sons, Inc., 1999.

Appendix: Inter-area Mode extractions of WECC event data using Prony and Matrix Pencil

Once the model structure is decided upon, the next step is to reconstruct the equivalent slow components of the voltage and phase angle signals available from the PMUs at the pilot bus of each cluster. In order to identify the mode content of pilot buses voltage, we used Prony and Matrix Pencil methods. In the following, the constructed pilot bus for each area and midpoint, and their mode contents are presented event by event. It should be noted that only voltage phase angles data are used for mode extraction because it represents the dynamic of the power system more clearly than voltage magnitude.

- **Feb-18-2011**

For this event, we do not have access to PGE and SRP data files, thus the midpoints are not considered in this event. Also, Eldorado is considered in AN instead of a separate midpoint. The following figures show the constructed voltage and phase angle data (the actual PMU data without any modal decomposition) for each of the pilot buses.

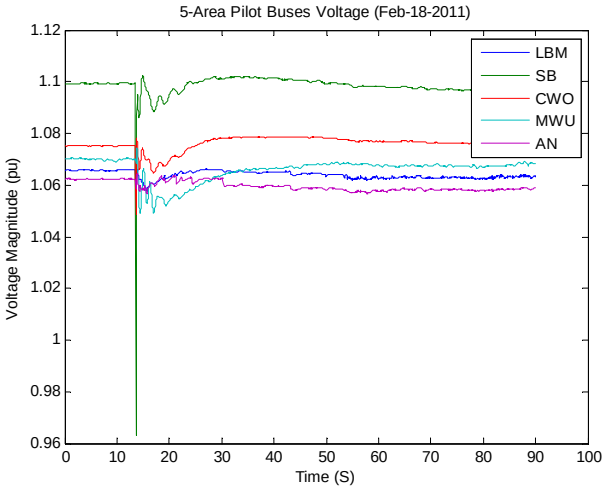

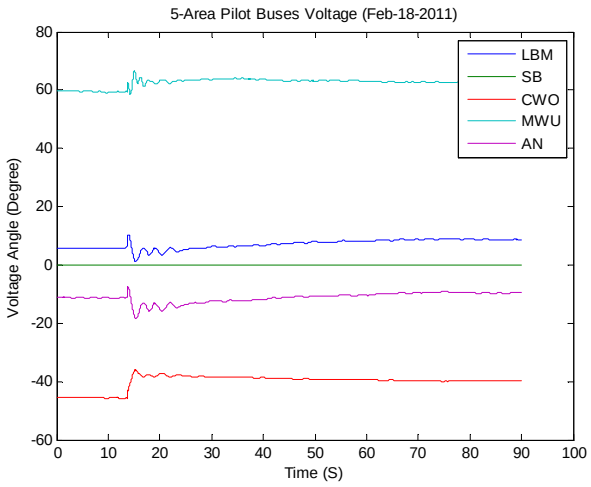

It should be noted that pilot buses voltage phase angles in this event and all other events are derived considering the phase angle of SB pilot bus, which is actually the phase angle of Malin, as phase angle reference. The modes with the frequencies within the interested range (between 0.1 and 1.0) are tabulated in Table 1. The orange column represents the results of Prony and the green column represents the result of Matrix Pencil method. It should be noted that in the following table and the other tables hereafter, F, D, and R refer to the real part, frequency, and the residue of a mode, respectively. This means that the share of a mode in a waveform is $Re^{-Dt}\left(\sin\left(2\pi Ft\right)+\cos\left(2\pi Ft\right)\right)$. Table. 1

Los Angeles - Baja - Mexico

F	D	R	F	D	R
0.391189121	0.224061196	1.75656154	0.179983697	15.9621164	282.3229574
0.222998531	0.168663496	0.969448508	0.374046056	0.156101494	1.416685986
0.576267846	0.338352237	0.600747857	0.230868706	0.129014263	0.692834081
0.822920155	0.435604732	0.345418338	0.137996684	0.115693245	0.430983676
0.175992026	0.103985827	0.343914554	0.666309693	0.151540487	0.134238494
0.188914517	0.05083073	0.166236638	0.240547815	0.015441481	0.103462578
			0.305307057	0.032133957	0.103410043
			0.364290098	0.007146855	0.087650721
			0.179257544	0.045985195	0.081256047
			0.473136284	0.087747534	0.078744185
			0.923176744	0.176516929	0.077634953

Canada - Washington -Oregon

F	D	R	F	D	R
0.376582414	0.363157968	1.932344356	0.356271798	0.225962958	1.292727285
0.261058918	0.291141597	1.06000836	0.234728893	0.193772046	0.842908082
0.541208968	0.772894025	0.791371781	0.835607014	0.336145869	0.178013128
0.214069158	0.215392049	0.397231889	0.336936193	0.052597453	0.105090979
0.835762051	0.552744881	0.236443125	0.519653457	0.086225849	0.088532063
			0.145460787	0.055940932	0.070615904
			0.503366461	0.057564324	0.043577261
			0.240647407	0.010754536	0.043089052

Montana -Wyoming - Utah

F	D	R	F	D	R
0.100595083	0.272793686	1.813665536	0.747031944	0.458417157	2.394566213
0.825855003	0.3718379	1.002388478	0.382115588	0.075374946	0.517543607
0.65992016	0.367325716	0.956650218	0.378582495	0.030440697	0.146195195
0.17310749	0.159280748	0.722421865	0.918866992	0.092020062	0.119337284
0.37052889	0.126803388	0.396135176	0.364996467	0.019724103	0.118413603
0.438791612	0.244572965	0.269689712	0.155369347	0.049316103	0.090722194
0.397988864	0.142453864	0.240521991	0.720331353	0.019379356	0.059640188
			0.24311386	0.185561482	0.054382835

Arizona - New Mexico

F	D	R	F	D	R
0.405690383	0.225971298	2.312193123	0.546246722	1.521753108	3.372250118
0.222774539	0.264512036	1.586014361	0.387662411	0.127323344	0.196592461
0.57189619	0.364639603	0.98582902	0.468879568	0.198168909	0.137061752

0.809324216	0.496348136	0.518570144	0.241618638	0.042510948	0.128934394
.445253498	0.150958923	0.502526039	0.872838564	0.247785841	0.054837856
			0.233339683	0.02904866	0.047714263

The following figures compare the original voltage phase angle and the approximate phase angle constructed by the dominant modes derived by Prony method. The dominant modes are DC modes, non-oscillatory modes (i.e. first-order or exponential modes that may result from PSS dynamics), and oscillatory modes with the residue equal or greater than 10% of the residue of the oscillatory mode which has the highest residue. Original phase angle data (with reference to Malin) vs 'effective slow component' for various clusters are plotted as follows:

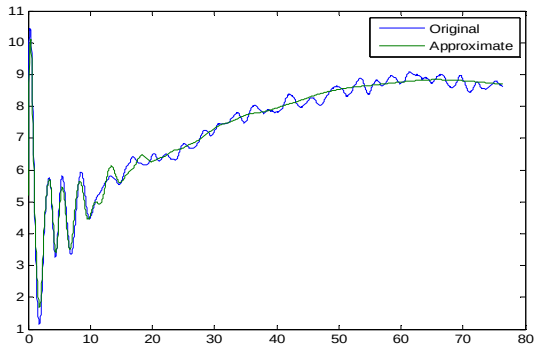

LBM

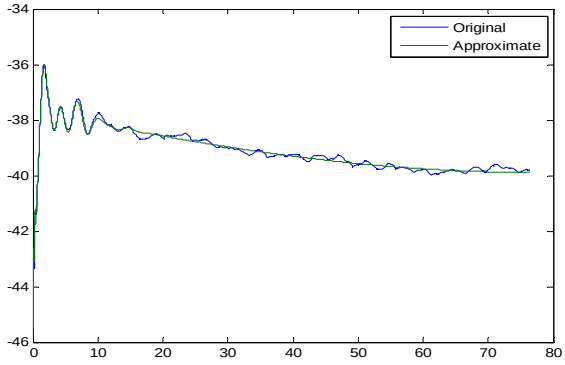

CWO

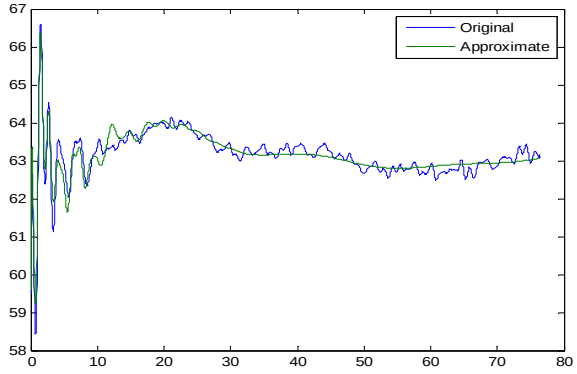

MWU

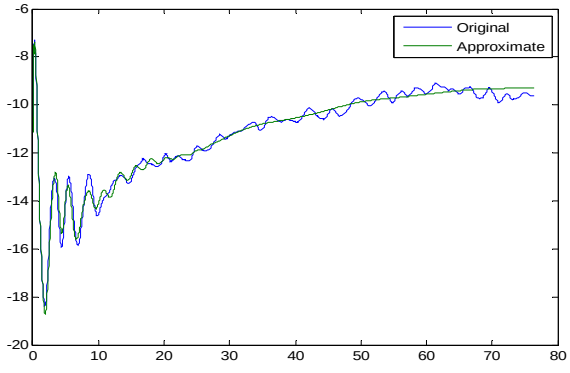

AN

Similar figures have been derived based on the modes derived using Matrix Pencil method. As it is evident from the above figures, the Prony method (and also Matrix Pencil) works well in identifying mode content of a waveform. The above figures have been derived for all events, however, for the sake of brevity, they are shown only for this event.

- **May-05-2011**

For this event, no data is available from AN area. Pilot bus voltage and angles, and their modal equivalents using Prony and Matrix Pencil have been derived.

- **Jun-05-2010**

For this event, we do not have access to PGE data files, thus the midpoint Diablo Canyon is omitted in this event. The following figures show the constructed voltage and angle data for all pilot buses.

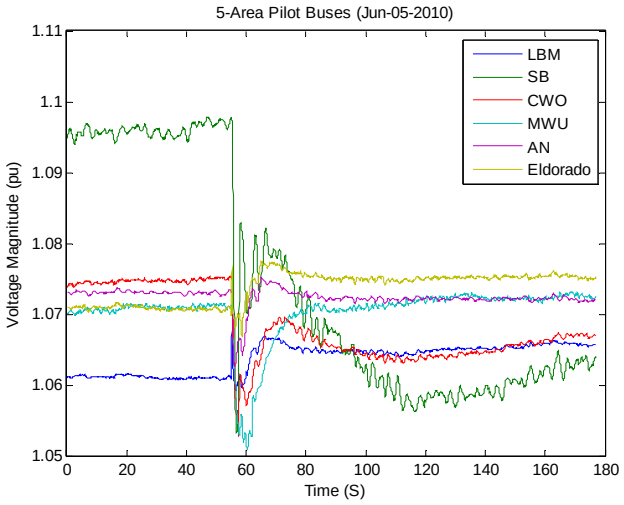

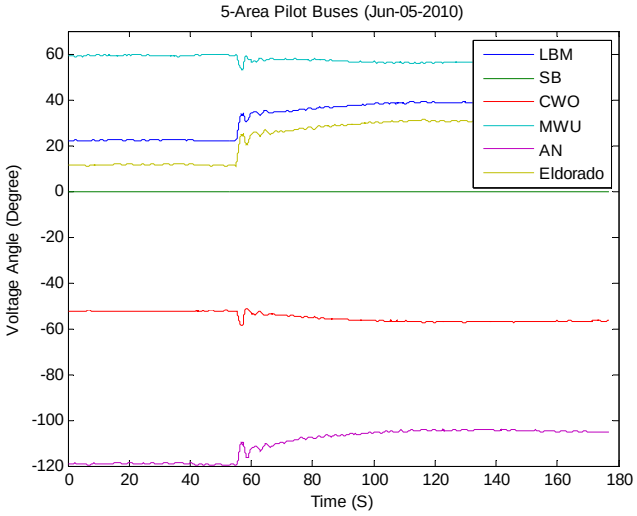

The modes with the frequenceis within the interested range (between 0.1 and 1.0) are tabulated as follows.Table 2

F	D	R	F	D	R
0.241949406	0.1601787	1.63904547	0.578657697	0.943937375	1.481205872
			0.234665155	0.167715521	1.196761419
			0.36302769	0.053032175	0.422778141
			0.365605722	0.173465224	0.393050365
			0.635058203	0.292250666	0.3410788
			0.401882355	0.045781844	0.332839042
			0.293566856	0.058364654	0.305958972
			0.448652833	0.06610452	0.235944187
			0.121671581	0.118555996	0.216895975
			0.727761267	0.134982168	0.161030962
			0.325391397	0.039147914	0.1492566

Canada - Washington -Oregon

Freq	Damp	Resid	Frequency	Damping	Residue

0.29238474	1.422946655	5.588764977	0.23964874	0.23888749	2.597399131
0.227109351	0.338741596	4.360635639	0.111591036	0.117852364	0.754818939
0.939961574	0.664228324	0.685309424	0.161151507	0.158023697	0.445484067
0.358814506	0.124605812	0.65666418	0.6702374	0.271254126	0.294219637
			0.118678252	0.071289601	0.291814982
			0.393360615	0.062951364	0.268201618
			0.409339049	0.061949868	0.252821655

Montana -Wyoming - Utah

F	D	R	F	D	R
0.29302264	4.617395961	5.834050902	0.260973053	0.220947612	1.824776939
0.375091414	0.229866545	1.154160113	0.87643656	0.35381542	0.915161203
0.29302264	4.617395961	5.834050902	0.74279054	0.061687823	0.552685122
0.375091414	0.229866545	1.154160113	0.742789154	0.037227519	0.320763048
			0.957093516	0.16681912	0.257477611
			0.333781584	0.086448962	0.250818223
			0.444320882	0.09691903	0.219368966
			0.694025036	0.051059493	0.209140978
			0.361266129	0.039376045	0.20812774

Arizona - New Mexico

F	D	R	F	D	R
0.985490906	0.713422923	1.978677019	0.547530406	1.404523601	8.825621065
0.238129914	0.152823023	1.715727825	0.365758297	0.173518504	1.812875288
0.926977474	0.451568957	1.391218645	0.219309454	0.089594152	0.869363265
0.603380556	0.281343292	0.871815329	0.29749385	0.071310895	0.813397482
			0.361677792	0.059869989	0.757833204
			0.401481975	0.06085694	0.68026857
			0.444388481	0.075025705	0.469047753

El Dorado

F	D	R	F	D	R
0.240286862	0.134314951	1.466397102	0.19996674	0.353858522	5.036900597
1.074738758	0.517125172	0.511350426	0.266356142	0.176412856	1.372703812
0.619035028	0.143373316	0.487988772	0.297173274	0.089230402	1.173122625
0.361669011	0.056656051	0.449343282	0.455161879	0.090643753	0.534000861
0.875985167	0.314754958	0.401137223	0.319940737	0.047738083	0.406716377
0.605331344	0.093979767	0.387021216	0.363764641	0.045028134	0.399684862
0.271347368	0.051191358	0.346638596	0.432045418	0.048552962	0.304293598
0.245422962	0.032283104	0.272321199	0.421260716	0.067413145	0.269711811

0.405174808	0.036527593	0.221792079	0.403106107	0.040838584	0.266446408
0.323254279	0.059132536	0.187385306	0.662940785	0.069885127	0.249902625
0.378312773	0.02977284	0.18508322	0.682101233	0.068599523	0.249553081
0.451264888	0.063691509	0.181879685			

- **Jun-18-2010**

For this event, complete set of data for each area is available. The following figures show the constructed voltage and angle data for pilot buses.

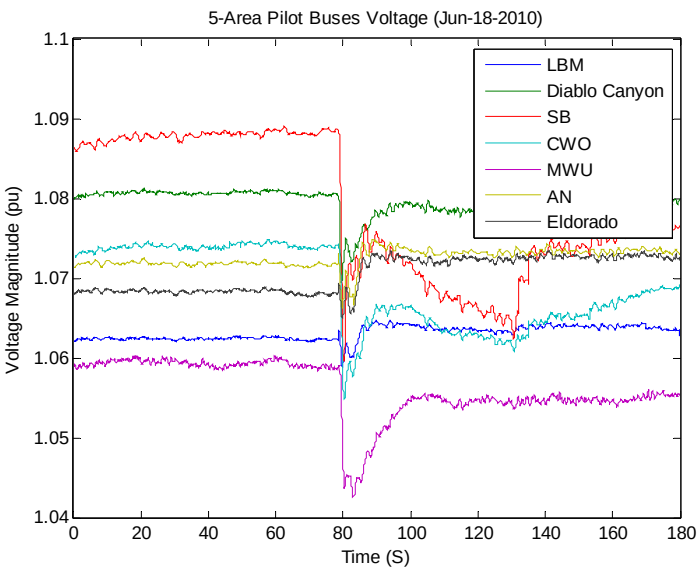

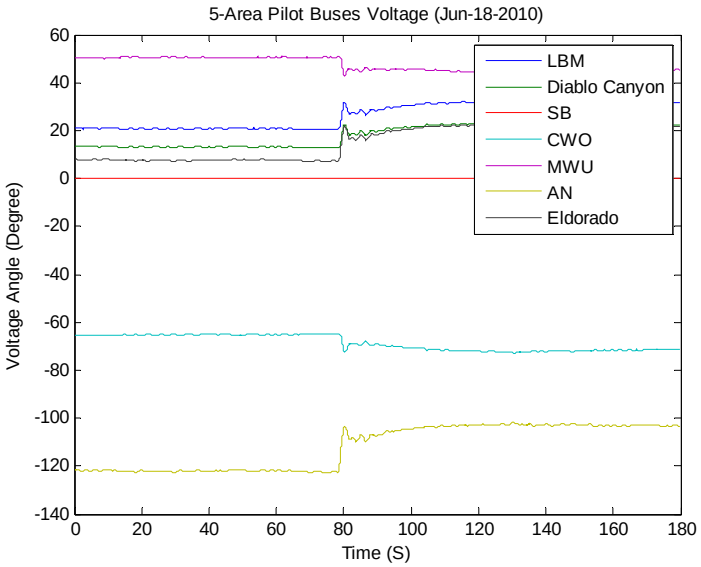

The modes with the frequencies within the interested range (between 0.1 and 1.0) are tabulated as follows.

Los Angeles Baja California Mexico

F	D	R	F	D	R
0.209555155	0.293665736	4.192451846	0.360782536	0.206563142	2.511264358
0.295515064	0.285165469	2.718829531	0.285387628	0.214901507	2.350578358
0.359767141	0.208553624	2.617228713	0.348107781	0.072041465	0.328154424
			0.615905998	0.084489327	0.235266868
			0.61004174	0.077202941	0.22294342

Diablo Canyon

F	D	R	F	D	R
0.224463112	0.333182051	5.311334299	0.25906143	0.278808556	2.715446942
0.323342128	0.666961194	4.313852422	0.323273386	0.110234889	0.600641837
0.336451667	0.150634428	1.951236598	0.379824672	0.067252884	0.390455929
0.35399122	0.088384287	0.792955114	0.628468298	0.496306968	0.343864984

0.587227917	0.906507244	0.692770217	0.555557262	0.171511888	0.149225362
			0.313907861	0.024126991	0.137135589
			0.111725222	0.037445122	0.135460621

San Francisco Bay Area

F	D	R	F	D	R
0.191167	0.479663055	6.619393686	0.173145146	0.627798705	7.782906773
0.366574835	0.172253349	1.554033204	0.359986717	0.313230765	3.074910964
0.25681897	0.142976201	1.203819174	0.288143626	0.169156608	1.90332168
0.281954203	0.094621488	1.162523771	0.389580181	0.059683214	0.686976308
			0.394784022	0.022608468	0.326476318
			0.450214909	0.219042823	0.216806836

Canada Washington Oregon

F	D	R	F	D	R
0.244746518	0.210807211	2.180132125	0.350506834	0.377011626	2.726792785
0.576811733	0.153685573	0.651586878	0.295594102	0.18078548	1.418528852
0.608416868	0.242074173	0.367353197	0.573730826	0.126062356	0.281091558
0.327906308	0.072670545	0.197852806	0.162613113	0.058194471	0.19230882
0.375711838	0.041028334	0.120366385	0.18825917	0.054375001	0.18720121
			0.145890358	0.071493295	0.179923535
			0.45420123	0.125797648	0.13906838

Montana Wyoming Utah

F	D	R	F	D	R
0.183791784	1.937063795	5.661987768	0.377947968	0.374896752	2.257300237
0.481501062	0.621740705	2.560136656	0.228838357	0.221490427	1.065147757
0.304470831	0.122352322	0.541104402	0.708449088	0.376789176	0.405430434
0.242584906	0.063215989	0.400999175	0.292122721	0.081473447	0.2874294
0.640028029	0.233195024	0.190803091	0.980724613	0.722316223	0.256501208
			0.237464184	0.037664665	0.151670704

Arizona New Mexico

F	D	R	F	D	R
0.223013023	0.264646943	4.059071728	0.261780303	0.259236329	3.047303078
0.353512723	0.198971492	2.36535039	0.314338243	0.130299621	1.61383493
0.338981874	0.848188062	1.881605508	0.385204992	0.125670699	1.303813651
0.281855356	0.047908421	0.335292113	0.317206036	0.03891457	0.319311018
			0.723366849	0.188720618	0.245605605

El Dorado

F	D	R	F	D	R
0.190257836	0.433854195	5.945489653	0.274217855	0.307466329	5.698738378
0.36751657	0.16973582	1.50716203	0.328853851	0.203122695	3.029677797
0.282859113	0.099695399	1.169534037	0.375412206	0.061247351	0.251947749
0.2601465	0.11439774	0.802856388	0.591969345	0.090581745	0.207612341
0.188443526	0.043965901	0.30985023			

- **Jun-23-2010**

For this event, complete set of data are available for all areas. The measurement data from Grand Coulee is erroneous; therefore the phase angle of Ashe has been chosen to represent the pilot bus phase angle of CWO area. The following figures show the constructed voltage and angle data for pilot buses.

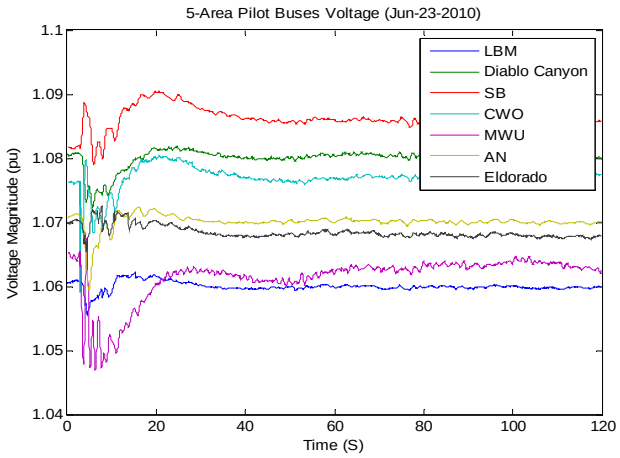

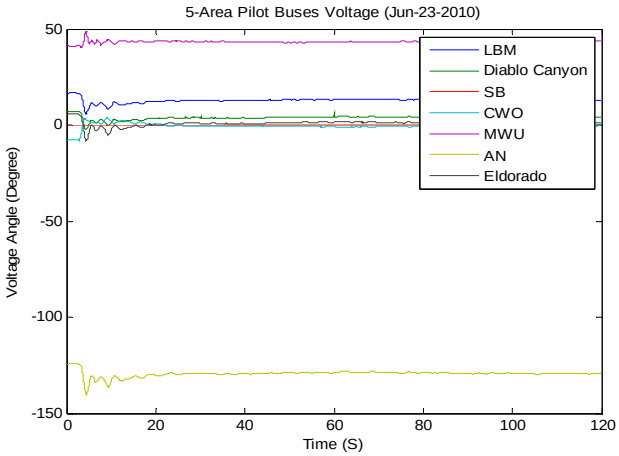

The modes with frequencies within the interested range (between 0.1 and 1.0) are tabulated as follows.

Table 4

Los Angeles Baja California Mexico

F	D	R	F	D	R
0.396854393	0.167540785	2.033674951	0.239426228	0.213260988	3.425909891
0.19841189	0.1745773	1.260809694	0.287286198	0.134377129	1.411107306
0.233413774	0.08499178	0.742353453	0.391319551	0.123819819	0.90205441
0.549388053	0.2848709	0.626995574	0.55497029	0.403081507	0.704199238
			0.31545147	0.069826046	0.384289184
			0.114922256	0.141135703	0.315163345

Diablo Canyon

F	D	R	F	D	R
0.392580048	0.15615651	1.394243822	0.399390021	0.45600027	2.026131382
0.209374237	0.167866928	1.060833264	0.19400148	0.351656601	1.462476435
0.232374774	0.093066993	0.818769709	0.240268585	0.095693139	0.512388795

0.573252794	0.441969191	0.662387897	0.390962497	0.101329009	0.369584605
0.713537284	0.171766019	0.215028142	0.795049499	0.356174718	0.235836676
0.320262467	0.0516918	0.127599528	0.227331482	0.065347718	0.206009893
			0.281450084	0.044574246	0.151962401
			0.313673921	0.050132346	0.149057314

Canada Washington Oregon

F	D	R	F	D	R
0.39159223	0.186094171	1.40762934	0.229164867	0.08349807	0.840299977
0.234636872	0.088422938	0.733896803	0.389211561	0.155583132	0.693794552
0.553063743	0.292198141	0.625606691	0.198346337	0.080164195	0.461397677
			0.852718556	0.689921508	0.432820748
			0.261587208	0.155939492	0.382386023
			0.212555522	0.050888598	0.271061788
			0.31529772	0.044253977	0.11271063
			0.573341211	0.109980623	0.098860574
			0.775528857	0.188887465	0.086500212

Montana Wyoming Utah

F	D	R	F	D	R
0.312844063	1.076333014	5.865554295	0.426541264	0.205217884	2.163512119
0.368337586	0.207842292	3.186550222	0.801081509	0.264916992	0.970644344
0.703018343	0.187868564	2.43504892	0.420153974	0.084663856	0.762567584
0.266696383	0.144919603	1.214541228	0.401977839	0.093723161	0.727918928
0.693858737	0.067188996	0.567722038	0.631842899	0.272937822	0.650842945
0.816779654	0.137320796	0.492662584	0.284969791	0.098670963	0.457561798
0.114434907	0.173696098	0.476293514	0.233754626	0.132009816	0.443276826
0.803383025	0.710055447	0.437319836	0.304472129	0.044168456	0.13411745
0.709382566	0.066238478	0.403473786			

Arizona New Mexico

F	D	R	F	D	R
0.385830167	0.18543295	2.801430236	0.38992991	0.172998279	2.527765119
0.221721152	0.219295481	2.390354916	0.204685349	0.262013456	2.282892388
0.545612306	0.326889731	1.724037128	0.528461231	0.317928844	1.492391391
0.114461692	0.261548158	1.443392797	0.225326857	0.067587849	0.329851565
0.594463344	0.499378828	0.551879201	0.23505204	0.045720175	0.32525534
0.151296433	0.112082192	0.452159388	0.283200067	0.038103946	0.192826886
0.23313831	0.053400725	0.409545211	0.543095193	0.066032627	0.178112462
0.283773004	0.0489851	0.270348648			

El Dorado

F	D	R	F	D	R
0.127182581	0.436906449	3.021206462	0.359407507	0.681209862	6.482759682
0.38627492	0.200877475	2.701734983	0.134007931	0.213030063	1.07241332
0.218844175	0.195636498	1.390042217	0.242426985	0.105500785	0.959441521
0.614679771	0.436433103	0.981214002	0.620724793	0.212551305	0.847663252
0.567314899	0.256028478	0.965389496	0.395935604	0.102894292	0.75320041
0.233330719	0.058219951	0.471336721			

- **Sep-27-2010**

For this event, no data from SRP is available and therefore, Eldorado is considered as the pilot bus of AN area, instead of a midpoint between AN and LBM areas. Also, the measurement data from Diablo Canyon is not available in the PGE file and hence, the midpoint Diablo Canyon is avoided. The following figures show the constructed voltage and phase angle for pilot buses. The modes with frequencies within the interested range (between 0.1 and 1.0) are tabulated as follows.

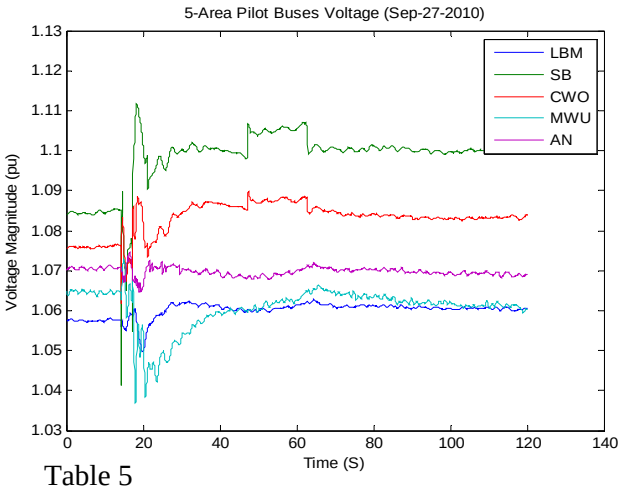

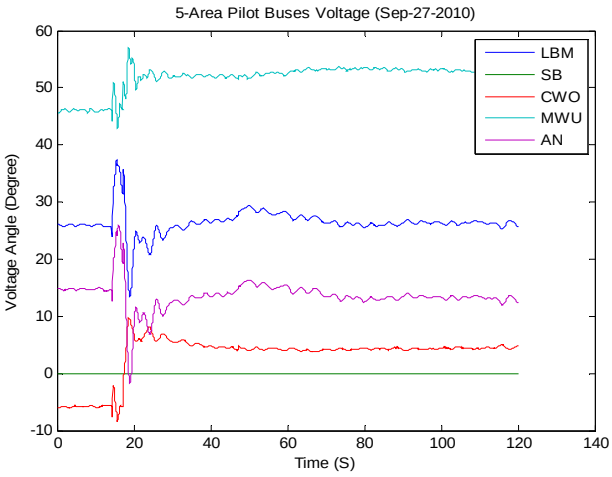

Table 5

Los Angeles Baja California Mexico

F	D	R	F	D	R
0.233377806	1.442813828	131.4508821	0.418835942	0.704763579	12.62351053
0.286908248	0.664148398	51.0446953	0.322948795	0.220030842	7.384314082
0.652612431	1.502773678	21.9642	0.150450382	0.284159069	6.605898774
0.106744661	0.317550112	9.311915511	0.836341972	0.569711936	2.952190998
0.387702543	0.415622272	9.111702199	0.236805839	0.096177258	1.921416117
0.894155096	0.667271703	4.256722036	0.3400578	0.106102232	1.311252814
0.240813894	0.090490905	1.714554344			

Canada Washington Oregon

F	D	R	F	D	R
0.262889491	0.605117662	20.62893266	0.271535436	1.12086991	23.16378048
0.34330169	0.415317192	6.87664517	0.311198135	0.306631866	5.071606597
0.241492554	0.105417783	1.666657644	0.238544537	0.119509017	2.107371283
0.98161064	0.494222265	0.898928067	0.904378787	0.433469759	0.888984097
0.767716413	0.272690984	0.471712928	0.833663824	0.218809939	0.342300717
			0.651734318	0.159767963	0.27384477

Montana Wyoming Utah

F	D	R	F	D	R
0.399906927	0.632339743	7.24234038	0.188684747	0.710092409	16.76686593
0.109939737	0.382951372	5.978075762	0.817951297	0.835606564	10.24353654
0.973071944	0.797468819	4.846429208	0.711651903	0.330971338	2.735694362
0.906258195	0.449341595	3.120980424	0.335655861	0.12520726	2.05453058
0.323719012	0.084751851	1.656000738	0.240656256	0.060948024	0.541895358
0.30937222	0.086658074	1.300354299	0.654557742	0.156155665	0.379682338
0.236889002	0.098815822	1.283647084	0.523150314	0.110948403	0.335176198
0.780313587	0.182887891	0.833125964	0.314260116	0.046185409	0.326937746

Arizona New Mexico

F	D	R	F	D	R
0.245529575	0.334044089	15.38311446	0.160900043	0.240915643	7.536421113
0.400325695	0.271998363	4.993453854	0.359558663	0.168725861	3.078158024
0.82765948	0.611332235	2.880697442	0.470492232	0.247344064	1.529014462
0.11950088	0.095642363	2.507671764	0.21694741	0.038942543	1.064303166
0.244168183	0.094182831	2.313411549	0.667493897	0.255811448	0.698112147

- **Nov-04-2010**

For this event, we do not have access to SRP and PGE data, therefore, the midpoints in Fig. 1 are discarded totally. Also, Eldorado is considered in AN instead of a separate midpoint. The following figures represent the voltage data for individual pilot buses.

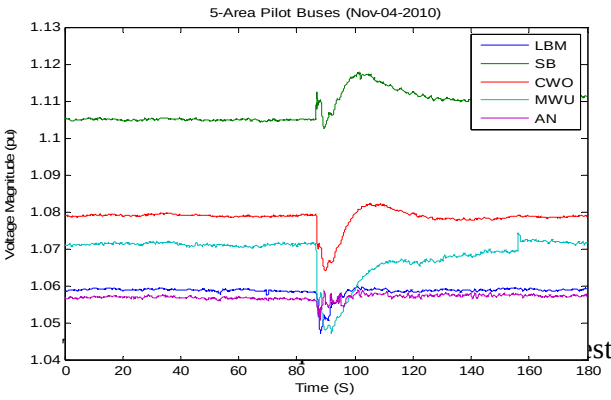

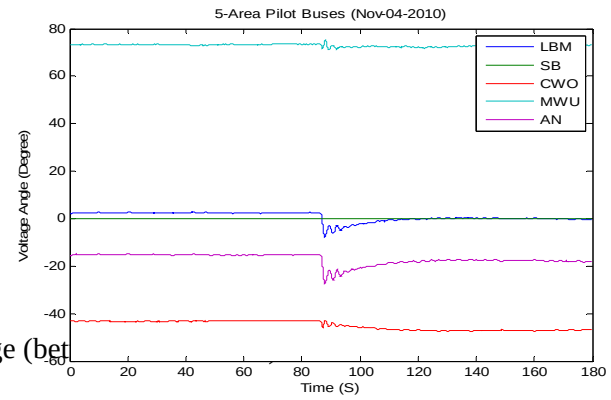

sted range (bet

Table 6

F	D	R	F	D	R
0.383898552	0.925469978	5.483495721	0.4103121	0.40141485	2.95347055
0.489570166	0.158984348	0.565448167	0.515353756	0.787991814	2.645920694
0.276653908	0.092035553	0.434844567	0.311608218	0.466953669	1.398176823
0.427933017	0.101058802	0.393191819	0.278504824	0.081980757	0.399840899
0.334266872	0.044929006	0.156642546	0.336323741	0.049472826	0.182384615
0.366115342	0.027032776	0.129950724	0.367798068	0.034861884	0.166688587

Canada Washington Oregon

F	D	R	F	D	R
0.440321981	0.400504637	1.502606427	0.436520025	0.621214519	2.261045833
0.156551603	0.551879415	0.83948133	0.274796685	0.107189559	0.419770514
0.271088668	0.096610061	0.365616533	0.827183515	0.498683924	0.179252358
0.244606419	0.028339624	0.144169836	0.512904888	0.079695291	0.169480379
			0.306061243	0.18034565	0.148691219
			0.245525836	0.023094629	0.119156472

Montana Wyoming Utah

F	D	R	F	D	R
0.69591168	1.067395041	1.073345337	0.536246489	1.528282389	3.225935086
0.44229723	0.321859773	0.912633964	0.369146801	0.407942333	1.898659498
0.108356894	0.115018481	0.494118772	0.767857181	0.155586894	0.281762031
0.406563294	0.147280773	0.476959984	0.142244742	0.083367356	0.267037143
0.82371257	0.262302121	0.37437694	0.922647928	0.371353076	0.229050594
0.863201249	0.083952377	0.192687904	0.167595258	0.162492414	0.220830404
0.275013095	0.047617689	0.144381746	0.841198694	0.199906821	0.207932573
0.365714011	0.028161106	0.090972922			

Arizona New Mexico

F	D	R	F	D	R
0.383006415	0.486807628	3.741872646	0.317912404	0.281731825	2.4178038
0.191410474	0.133468371	0.376606365	0.332968207	0.069245775	0.524321588
0.280924512	0.064021737	0.362000265	0.189729159	0.144448044	0.471671511
0.33532958	0.050447955	0.240397415	0.365942527	0.037789191	0.260586584
			0.310104577	0.018319223	0.124753986

As can be seen from the above tables, the frequency of the modes identified from Prony and Matrix Pencil algorithms are not necessarily the same for the same signal. The damping of each identified model is also different, but the curve fits are the same. In the estimation results listed in Section 5 we use the results of the Prony algorithm as it gives better curve fit with the measured data.